

Master Thesis:

Global models of substorm dynamics from satellite magnetic field measurements

AUTHOR:

MARIE VIGGER ELDOR - s164051

SUPERVISORS:

PROF. CHRISTOPHER CHARLES FINLAY (DTU)

POSTDOC CLEMENS KLOSS (DTU)

Date: January 2, 2022



Cover photo: Combination of ESA images [https://www.esa.int/ESA_Multimedia/Missions/Swarm/\(sortBy\)/view_count/\(result_type\)/images](https://www.esa.int/ESA_Multimedia/Missions/Swarm/(sortBy)/view_count/(result_type)/images) & [https://www.esa.int/ESA_Multimedia/Keywords/Description/Aurora_Borealis/\(result_type\)/videos](https://www.esa.int/ESA_Multimedia/Keywords/Description/Aurora_Borealis/(result_type)/videos)

Abstract

This thesis presents a model of the ionospheric currents for geomagnetically disturbed times based on data from the satellite mission Swarm accompanied by auxiliary data on solar wind conditions and data from ground magnetometers. The model is derived using the ionospheric currents modelling procedure of AMPS (Laundal, Finlay, Olsen, and Reistad 2018) and is implemented in the Python software Multifit (Kloss 2021). The *SML* index is a measure of the auroral electrojet activity derived from ground magnetometers; in a departure from the original AMPS approach it is here included as an additional input and found to be a crucial controlling parameter for the models presented.

Using ESA’s Swarm satellite mission magnetic data from the years 2014 to 2017 was used to produce a series of models of the horizontal divergence-free ionospheric currents (DFC) and field-aligned currents (FAC). These models were derived using a robust regularised least squares method. It is shown to be possible, using this approach, to model the radial component of the ionospheric field, B_r^{ion} during disturbed conditions, to an accuracy within 40-50nT. However modelling the southward B_θ^{ion} and eastward B_ϕ^{ion} field components is found to be more difficult due to the influence of the highly dynamic and small-scale FACs that are not well captured by the model. During a large substorm event, the models show that the structures of the DFCs evolve as the time progresses. At the beginning of the substorm the DFCs have a very complex pattern but as time elapses the pattern starts aligning with the FACs and gains a more defined structure where the negative parts of the DFC gather around the upward FAC and the positive parts of the DFC gather around the downward FAC. The model also shows, as expected, that the maximum amplitude of the horizontal sheet current density of the ionosphere, moves southwards to lower magnetic latitudes during the substorm.

For validation purposes the model predictions are compared to independent data from the satellite and ground observatories. The results of this comparison show that the model predictions follow the same general patterns as the independent satellite data although it fails to reach the same amplitudes. This may partly be a consequence of the model lacking information concerning substorm activity due to the relatively short timespan of the input Swarm data. By expanding the dataset it should be possible to better train the algorithm to model substorm dynamics by basing it on a wider range of events. The comparison to ground observatory data shows that the model deviates significantly, both in amplitude and pattern, from the measured data. This is due to unresolved small scales or non-typical dynamical features in any given substorm and the un-modelled induced currents in the mantle. In future models it is recommended to include ground observatory data along with satellite data when deriving the model, to account for the induced currents, and to consider including new input parameters e.g. the amount of open magnetospheric flux. It is also discovered that the chosen a-priori data error, $\sigma = 40\text{nT}$, seems to be an underestimate for the components B_θ^{ion} and B_ϕ^{ion} ; it is suggested to apply individual a-priori errors to

the different field components in the future. The distributions of residuals, between model and Swarm data, appear to be Laplacian distributed, whereas Huber weights were used in this thesis. It is recommended to investigate whether a Laplacian weighting-scheme could improve the accuracy of the model.

Acknowledgements

I would like to thank my two supervisors Chris Finlay and Clemens Kloss for their knowledge, guidance, and support during these last five months, I have been very happy to be a student of yours. I would also like to thank the division of Geomagnetism and Geospace for creating a very welcoming environment and a special thanks to Anna Willer for introducing me to the world of geomagnetism and space weather. Also thank you to my friend and colleague Linda Christoffersen for your bold feedback and good company. Finally a huge thank you to my parents for supporting me in every way throughout my education.

Contents

1	Introduction	1
1.1	Aim of the thesis	1
2	Earth's magnetic field - background theory	6
2.1	Magnetic sources	6
2.1.1	Internal sources	7
2.1.2	External sources	7
2.2	Geomagnetic disturbances	10
2.2.1	Substorms	10
2.2.2	Magnetic activity indices	11
2.3	Representing the ionospheric current system	12
2.3.1	Apex coordinate systems	12
2.3.2	The geomagnetic elements	13
2.3.3	Maxwell's equations	13
2.3.4	Modelling the ionospheric magnetic field: AMPS	14
2.4	Model parameter estimation	17
2.4.1	Multifit	19
3	Observations	20
3.1	Swarm data	20
3.2	Ground stations and observatories	22
3.3	Data selection	24
3.3.1	Selection of disturbed conditions using <i>SML</i> index	24
4	Results	29
4.1	A model of the polar ionospheric field during disturbed conditions	29
4.1.1	Model setup	29
4.1.2	Fit of model to Swarm data	29
4.1.3	Typical model properties and ionospheric currents during disturbed conditions	33
4.2	Dynamics during substorms	36
4.3	Comparison with independent observations during an example substorm event	40
4.3.1	Comparison to independent satellite data	41
4.3.2	Ground observatory comparison	42
4.4	Testing alternative datasets	44

5	Discussion	48
5.1	Fit of Model A to Swarm data	48
5.2	Evaluation of model performance under typical conditions	49
5.3	Evaluation of model performance during substorms	49
5.4	Fit of Model A to independent data	50
5.5	Controlling factors in the model	50
5.6	The influence of data selection	51
5.7	Recommendations and Future work	51
6	Conclusion	53
	Bibliography	55
A	Model construction and setup	57
A.1	Regularisation of FAC	57
A.2	Choice of truncation level m	60
A.3	Choice of truncation level n	61
A.4	Test of convergence	62
A.5	Test of a-priori data error	62
A.6	Construction of Model B	64
B	Scripts	65

Introduction

For centuries scientists have tried to explain the peculiar phenomena that give rise to the sources of Earth's magnetic field. While the causal observer is bedazzled by the beauty of polar lights researchers have strived to fully explain the electromagnetic mechanism behind the phenomenon. This is not an easy task since the magnetic field is made up by a variety of different sources both in- and outside the Earth [Olsen and Stolle 2012]. In particular sources above the Earth's surface, e.g. the ionospheric field, have proven to be particularly complicated to model since they may be rather localised in space while vary rapidly in time.

During geomagnetically disturbed times the ionospheric currents make up a complex system that consists of both horizontal sheet currents and field-aligned, also known as Birke-land, currents [Kelley 2007]. Due to the highly dynamical nature of the polar ionosphere, which is mainly driven by the solar wind's interaction with the Earth's magnetosphere, modelling the currents during disturbed times can be very challenging. Yet these disturbed conditions, with their associated strong ionospheric currents, are also the most important to understand both from the standpoint of space weather applications and for the fundamental understanding of solar-terrestrial coupling.

1.1 Aim of the thesis

The aim of this thesis is to derive a climatological model of the ionospheric currents during magnetically disturbed times. The model will be based on the average magnetic field and polar current system (AMPS) modelling scheme (Laundal, Finlay, Olsen, and Reistad 2018), but for the purpose of this thesis a measure of the auroral electrojet activity, known as the *SML* index, is introduced as an additional input parameter in the modelling scheme. Furthermore, the model will be based on magnetic data from ESA's Swarm A satellite obtained in the time interval of 01/01/2014 to 31/12/2017 and additional auxiliary data on solar wind and interplanetary magnetic field conditions.

DTU's python software for geomagnetic field modelling, called Multifit [Kloss 2021], will in this thesis be used to produce the ionospheric current models based on data from Swarm A from geomagnetic disturbed times.

Chapter 2 will introduce the basic principles and methodology used in this thesis. Chapter 3 will present the properties of the dataset used for the modelling procedure and show

how geomagnetic disturbed times are selected. Chapter 4 presents the results of the model including the performance during typical conditions and during substorm events. Comparisons to independent data sources e.g. satellite and ground observatory data will be conducted as well and in chapter 5 the findings will be discussed and recommendations to future work will be proposed. A summary and conclusion can be found in chapter 6.

Symbols and notation

Abbreviations	Description
AE	Auroral electrojet indices
AL	Auroral activity indices
AMPS	Average Magnetic field and Polar current System
AU	Auroral activity indices
ASM	Absolute scalar magnetometer
CHAOS	Time-dependent geomagnetic field model (acronym pointed to CHAMP, Ørsted and Scientific Application Satellite-C (SAC-C))
DFC	Divergence-free currents
ESA	European Space Agency
FAC	Field-aligned currents or Birkeland currents
HRN	Ground observatory in Norway
IGRF	International Geomagnetic Reference Field model
IMF	Interplanetary magnetic field
LEO	Low Earth orbit
LS	Least-squares
MA	Modified-Apex coordinate system
MLT	Magnetic local time
MGD	Ground observatory in Russia
QD	Quasi-Dipole coordinate system
R1	Region 1 currents
R2	Region 2 currents
RMS	Root-mean-square value
SH	Spherical Harmonics
SOD	Ground observatory in Finland
SME	Electrojet index for magnetic activity
SML	SuperMAG version of AL index
SMU	SuperMAG version of AU index
STR	Star tracker
VFM	Vector field magnetometer

Symbol	Description
a	Mean radius of Earth
\mathbf{B}	Magnetic flux density or simply the magnetic field
B_e	Component of \mathbf{B} in the geodetic east direction
B_{IMF}	IMF strength
$B_{IMF,y}$	IMF component in the y-direction
$B_{IMF,z}$	IMF component in the z-direction
\mathbf{B}^{INT}	Internal magnetic field
\mathbf{B}^{ion}	Ionospheric magnetic field
\mathbf{B}^{mag}	Magnetospheric magnetic field
B_n	Component of \mathbf{B} in the geodetic north direction
\mathbf{B}_{NEC}	Magnetic field vector in Earth entered coordinates
\mathbf{B}^{pol}	The magnetic poloidal field for the ionosphere
B_ϕ	Component of \mathbf{B} in the ϕ direction
B_r	Component of \mathbf{B} in the radial direction
B_θ	Component of \mathbf{B} in the θ direction
\mathbf{B}^{tor}	The magnetic toroidal field for the ionosphere

B_u	Component of \mathbf{B} in the geodetic up direction
c	Tunning constant
\mathbf{C}_d	Data covariance matrix
\mathbf{C}_m	Model covariance matrix
D	Declination
\mathbf{d}	Data vector for the forward problem
$\mathbf{d}_1, \mathbf{d}_2$	MA base vectors
$dSML_{abs}$	The absolute change in SML index
$dSML_{limit}$	SML change limit
\mathbf{E}	Electric field
\mathbf{e} or e_i	Residual vector or individual residuals
\mathbf{E}^P	Direction of flow for Pedersen currents
F	Field intensity or field strength
F_m	magnitude of the cross product between \mathbf{f}_1 and \mathbf{f}_2
$\mathbf{f}_1, \mathbf{f}_2$	Base vectors
$F_{10.7}$	Solar radio flux index
\mathbf{G}	Design or kernel matrix for the forward problem
g_n^m	SH coefficient of degree n and order m for the potential field V
H	Horizontal field intensity
h	Altitude from the Earth's surface to the point of the measurement
h_A	Geodetic height of the field line apex
h_n^m	SH coefficient of degree n and order m for the potential field V
h_R	Fixed reference height
I	Inclination
\mathbf{I}_d	Identity matrix
I_m	Mathematical operation for the toroidal potential
\mathbf{J}	Electric current density in units A/m ²
J_{FAC}	Current density for the FAC
J_H	Horizontal sheet current density
$J_{H,DFC}$	Horizontal sheet current density produced by the DFC
$J_{H,FAC}$	Horizontal sheet current density produced by the FAC
J_r	Current density for the radial currents
J_u	Current density for the upward currents
\mathbf{k}	Unit vector relative to the ellipsoid
K_p	Global geomagnetic activity index
m	SH order or truncation level
\mathbf{m}	Model parameter for the forward problem
m_{DFC}	SH order for the DFC
\mathbf{m}_{dipole}	unit vector in the direction of the magnetic dipole axis
m_{FAC}	SH order for the FAC
$misfit_{norm}$	Normalised misfit
$model_{norm}$	Model norm
N	Number of datapoints
n	SH degree or truncation level
n_{DFC}	SH degree for the DFC
n_{FAC}	SH degree for the FAC
n_t	A constant that defines the number of data points in the time interval from t_0 to $t_0 + t_{ql}$
P	Poloidal potential
P_n^m	Legendre functions of degree n and order m for the potential fields

R	Distance from satellite to center of the Earth in km
\mathbf{r}	Unit vector
RC	RC index of magnetospheric ring current
RC_e	External RC-index
RC_i	Internal RC-index
\mathbf{s}	unit vector pointing in the direction of the Sun
T	Toroidal potential
t_0	Time of substorm onset
t_{ql}	Quiet limit
V	SH potential
v_x	Solar wind speed
\mathbf{W}	Weight matrix
\mathbf{w}_{huber}	Vector containing Huber weights
X	Component of \mathbf{B} pointing towards geographic North
Y	Component of \mathbf{B} pointing towards geographic East
Z	Component of \mathbf{B} pointing vertically downwards

Greek symbols	Description
α^2	Regularisation parameter of the FAC
β_{tilt}	Dipole tilt angle
$\delta\mathbf{m}$	Change in model parameters
ϵ	Solar wind magnetospheric coupling function
ϵ_0	Vacuum permittivity $8.8541878176 \cdot 10^{-12} \text{As/Vm}$
η_n^m	SH coefficient of degree n and order m for toroidal potential
θ	Colatitude in degrees
θ_c	IMF clock angle in degrees
$\mathbf{\Lambda}$	Regularisation matrix
λ_m	Latitude in MA coordinates
λ_q	Latitude in QD coordinates
μ_0	Magnetic permeability of the vacuum $4\pi \cdot 10^{-7} \text{Vs/Am}$
ρ	Density of electric charges in units of As/m^3
σ	Standard deviation or data error
τ	Solar wind-magnetospheric coupling function that deals with lobe reconnection rate on the night-side of the magnetotail
Φ	Loss function
ϕ	Longitude in degrees
ϕ_{MLT}	Longitude for magnetic local time
ϕ_{noon}	Apex longitude of the magnetic meridian
ψ_n^m	SH coefficient of degree n and order m for toroidal potential

Earth's magnetic field - background theory

2.1 Magnetic sources

Earth's magnetic field is a complex system that spans from the interior of the Earth and reaches out far beyond the Earth's surface. In fact the magnetic field of Earth extends far out into space. Further out in the heliosphere, where the solar wind dominates, positively and negatively charged particles make up an ionised gas.

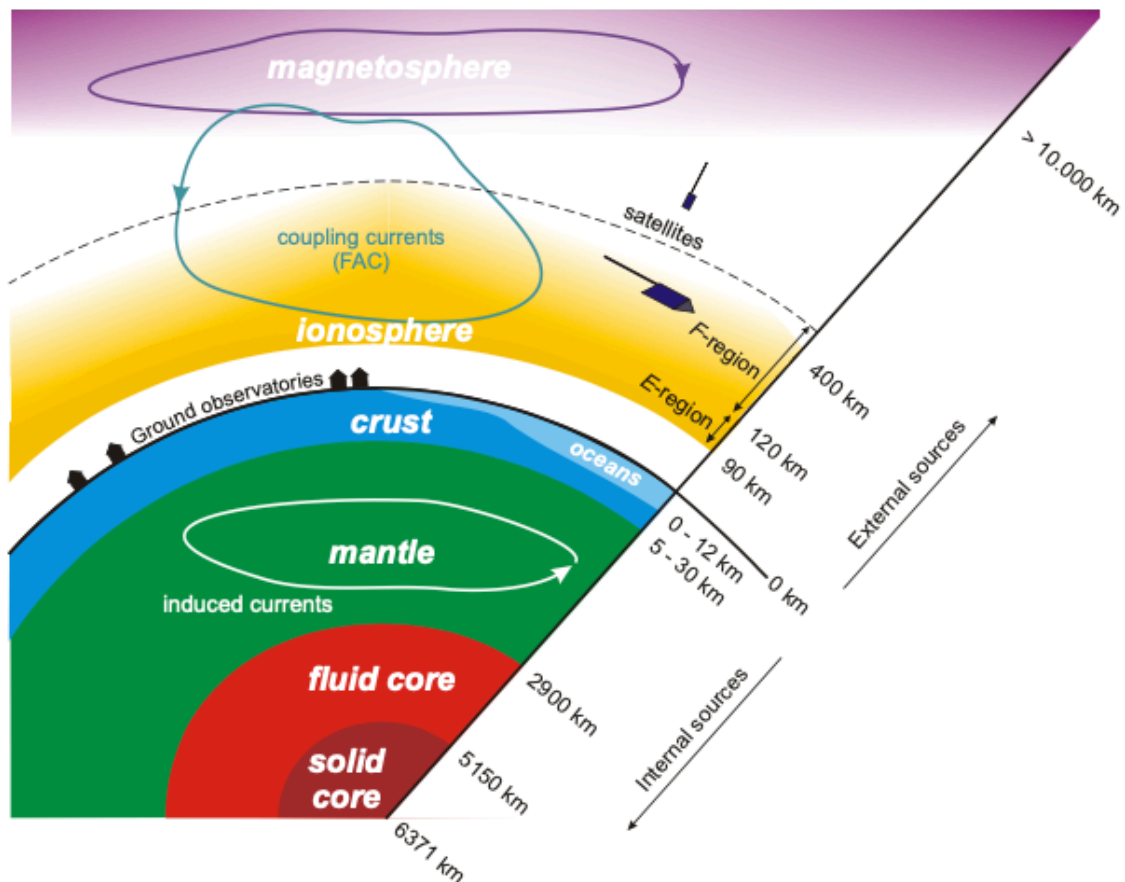


Figure 2.1: Near-Earth geomagnetic field sources from Olsen and Stolle 2012, seen from an observer on the Earth's surface.

As these particles approach the Earth they interact with the internally generated magnetic field. This causes the particles to move and generate disturbances in the magnetic field [Baumjohann and Nakamura 2007]. This chapter will introduce the present state of theory regarding contributions to the magnetic field of Earth including magnetic fields with origins internal and external to Earth's surface, with a focus on ionospheric fields and how to model these. Figure 2.1 displays the different regions that all contribute to the magnetic field of Earth.

2.1.1 Internal sources

The internal sources of the Earth's geomagnetic field are defined as the sources that are below as seen by an observer. The observer can for instance be a magnetometer on board a satellite or a ground based magnetometer station.

The outer core field

The core field, also known as the Earth's main field, makes up for more than 94% of the total magnetic field of Earth [Olsen and Stolle 2012]. The core field is produced by motions of the liquid outer core that consists of molten iron alloy. The temperatures in this region greatly exceed the Curie temperature hence no magnetised material can exist here. The molten iron has the viscosity of water and it is much hotter in the center of the planet thus thermal convection can take place. This gives rise to currents that drive the dynamo action that produces and sustains the magnetic field [Christensen and Wicht 2015].

The mantle field

The mantle is a solid layer in the Earth that mainly consists of rocks and minerals. The temperature in the mantle also exceeds the Curie temperature hence the mantle is a non-magnetic region. In contrast to the outer core, there is no movement of electrical conducting material and thus no dynamo action. However the mantle still contributes to Earth's magnetic field. Due to time-changes in the ionospheric and magnetospheric magnetic field, secondary electromagnetic induced currents in the conducting mantle appear [Constable 2015].

The lithospheric field

The lithospheric field, also known as the *crustal* field, is the geomagnetic field caused by magnetised material in the Earth's crust. When a magnetic material cools down through the Curie temperature magnetism in the material can arise. In the crust this is the case. The magnetic field arising from this process makes up for 3% of the total magnetic field at the Earth's surface.

2.1.2 External sources

The external geomagnetic sources are characterised as all geomagnetic sources that are above the observer. Figure 2.2 shows the external sources. The following sections will describe the origin of the outer geomagnetic field.

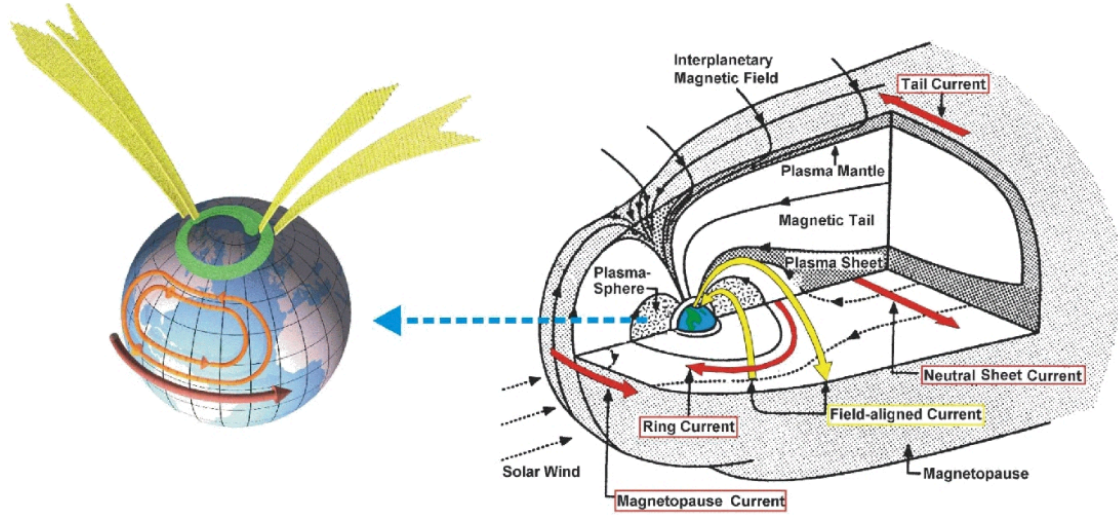


Figure 2.2: The left image illustrates the major current systems in the ionosphere, while on the right is shown the current systems in the magnetosphere. The yellow lines are the field-aligned currents (also known as Birkeland currents) while the orange lines represents the solar quiet currents in the ionospheric E-layer and the green line is the auroral electrojet, also in the E-layer. The image is taken from “Lecture notes, MSc Geomagnetism course, DTU” 2021.

The magnetospheric field

The Sun plays an important part in the external magnetic field. It emits plasma into the surrounding space. This highly conducting plasma is what we know as the *Solar wind*. The solar wind has a typical velocity of about 500km/s and is made mostly of electrons and protons [Baumjohann and Nakamura 2007]. The solar wind cannot simply penetrate the magnetic field of Earth and when it gets near it, it gets deflected. The speed of the solar wind is so high that when it “hits” the magnetic field of Earth a *bow shock wave* is produced, see figure 2.3a. Thermal energy is created in this process as the particles from the solar wind get slowed down, this plasma is situated in the *magnetosheath* [Baumjohann and Nakamura 2007].

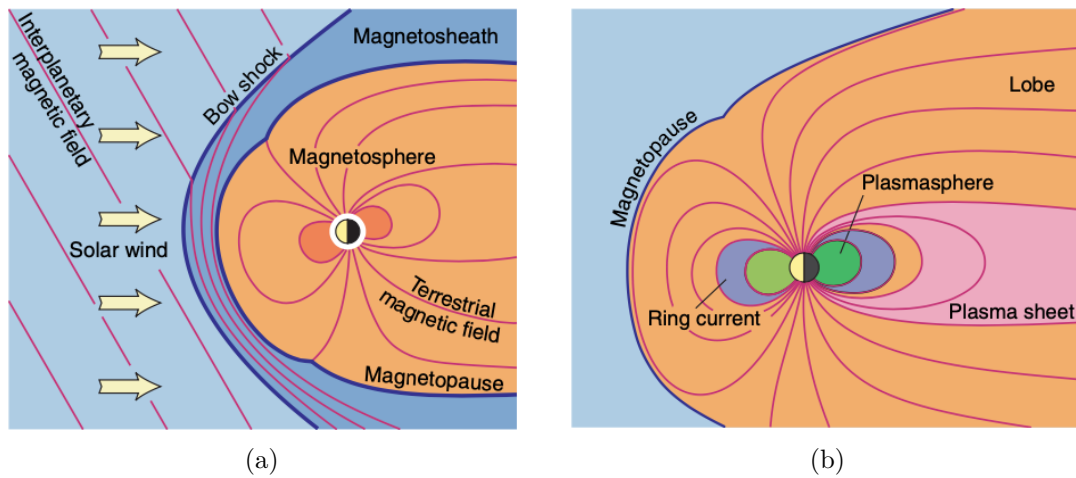


Figure 2.3: Interaction between the solar wind and the magnetic field of Earth (a) and an illustration of the different regions in the external magnetic field. Figures reprinted from Baumjohann and Nakamura 2007.

The *magnetopause* separates the interplanetary magnetic field (IMF) lines and the terrestrial magnetic field lines. The cavity in the solar wind created by the planet's own magnetic field is called the *magnetosphere* [Baumjohann and Nakamura 2007].

The solar wind generates a pressure that pushes the terrestrial dipole-like field to take a new shape. On the day-side the field gets more compact and on the night-side the shape of the field gets dragged out in to a tail-like shape called the *magnetotail* [Baumjohann and Nakamura 2007]. The magnetospheric field is connected to the ionosphere through field-aligned currents, also known as Birkeland currents.

The ionospheric field

The ionosphere is a region in the upper atmosphere where charged particles exist. When the solar wind interacts with the Earth's internal magnetic field it sets the charged particles in motion and this is the main driver of the ionospheric field.

The ionospheric field is a three-dimensional current system. In this thesis I decompose the currents into field aligned currents (FAC) and horizontal sheet currents. The horizontal sheet current is two dimensional and consist of Pedersen and Hall currents generated by the FAC and the divergence free currents (DFC) respectively [Laundal, Finlay, Olsen, and Reistad 2018].

During highly geomagnetic disturbed times the FACs form two ring-shaped currents near the auroral oval [Milan et al. 2017]. The inner ring *Region 1*, denoted R1, is the strongest ring and at dawn the current here is directed downward and at dusk the current is directed upward.

The outer ring is called *Region 2* (R2) and here the current is directed upward at dawn and downward at dusk, see figure 2.4. At polar latitudes, which is the focus of this thesis, the field-aligned current density J_{FAC} is approximately equal to the upward or vertical current density J_u :

$$J_u \approx J_r \approx J_{FAC} \quad (2.1.1)$$

where J_r is the radial current density. u denotes the magnetic upward direction which at the North pole is very close to the geodetic up.

The ionosphere consists of three main regions: the D-layer (extends from 60km-90km), the E-layer (extends from 90km-150km), and the F-layer (extends from 150km-500km) [Kelley 2007]. When the FACs enter the E-layer, at

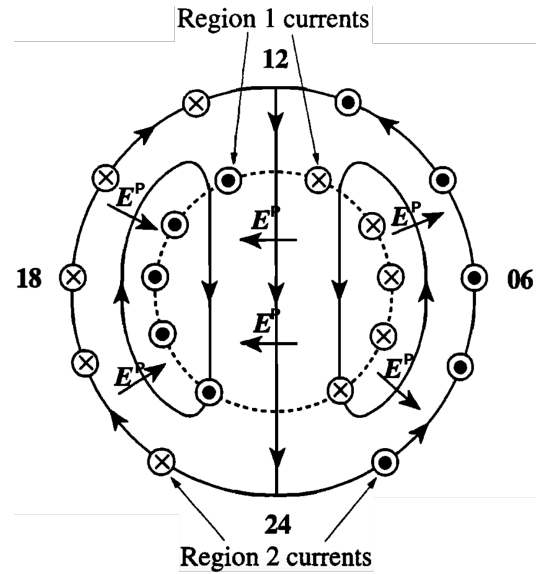


Figure 2.4: A sketch showing the currents in the polar ionosphere (reprinted from Cowley 2000). The dashed lines represents the polar gap boundary while the solid lines illustrates the plasma flow. "12" indicates noon while "24" is midnight and dawn on the right and dusk on the left. "⊙" indicates upward FAC and ⊗ indicates downward FAC. \mathbf{E}^P indicates the direction of flow for the Pedersen currents.

an altitude of approximately 110km, J_r is transformed into a horizontal current density $J_{\mathbf{H},FAC}$ which drives the Pedersen current. Combining this current density with the Hall currents created by the divergence-free part $\mathbf{J}_{\mathbf{H},DFC}$, the total horizontal sheet current density can be described as:

$$\mathbf{J}_{\mathbf{H}} = \mathbf{J}_{\mathbf{H},DFC} + \mathbf{J}_{\mathbf{H},FAC} \quad (2.1.2)$$

The currents in the E-layer are below satellite altitude but above the Earth's surface making the ionosphere an internal source for satellite observations but an external source for ground observations. For observations taken at the surface the most predominant field perturbations are caused by the DFC and the induced currents below ground. For measurement taken from higher altitudes the FACs also play an important role [Kelley 2007].

2.2 Geomagnetic disturbances

At high-latitudes the FACs connect the ionospheric currents to the magnetospheric currents. Hence the dynamics of the ionosphere is heavily controlled by the dynamics of the magnetosphere.

When the IMF has a southward component the field lines can merge with the terrestrial field lines on the dayside of the magnetopause [Baumjohann and Nakamura 2007]. This will create open field lines that the solar wind will transport across the polar cap. On the nightside of the magnetosphere the open field lines will reconnect causing magnetic tension. To release this tension the stretched field lines will transport plasma back towards the Earth [Baumjohann and Nakamura 2007]. Figure 2.5 illustrates this phenomenon.

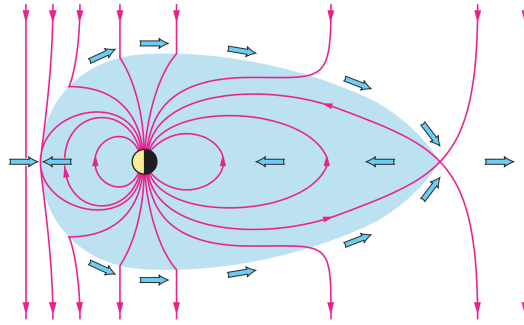


Figure 2.5: The sketch shows the reconnection and convection phase in the magnetosphere for southward IMF, reprinted from Baumjohann and Nakamura 2007.

This system will generate ionisation in the Auroral oval which lies as a band around the polar cap. This is where the auroral electrojets are formed. The so-called convection electrojets consist of a westward and eastward components which are mainly controlled by the FACs [Baumjohann and Nakamura 2007]. Indices such as AE , AU and AL are used as a measure of polar electrojet activity, section 2.2.2 will describe this in more detail.

2.2.1 Substorms

During times of high solar activity the enhancement in the merging rate sends flux from the dayside of the magnetopause into the magnetotail. Here some of the flux is reconnected and returned to the dayside, but not all. The rest of the flux accumulates in the tail lobes. When too much flux, or magnetic energy, has compiled in the tail lobes, typically after 30-60min, the tail becomes unstable and is forced to release the energy [Baumjohann and Nakamura 2007]. This release of stored magnetic energy from the tails is known as a substorm. At this time more intense polar lights will be seen in the auroral oval.

During a substorm an enhancement of the ionospheric currents can be measured, in particular regarding a strengthening in the westward substorm electrojet at the midnight sector. The substorm current wedge arises from the coupling between the magnetosphere and the westward currents through FACs on either side of the local midnight sector [Kepko et al. 2015].

2.2.2 Magnetic activity indices

Magnetic activity indices have been developed in order to characterise magnetospheric activity. The AL index has been used in relation to substorm activity and is often used to monitor the strength of a substorm [Newell and Gjerloev 2011]. The AL index is derived using magnetic data obtained by 12 ground stations in the Northern polar region. Despite the advantages of AL the utilisation of the index has been limited due to uncertainties in the index that stems from the limited number of ground stations. Newell and Gjerloev 2011 chose to refer to the originally derive index as *Auroral Electrojet* $AE(12)$ (12 stands for the 12 ground stations used) and it is computed by using the largest value $AU(12)$ of the horizontal component H and the lowest value $AL(12)$ of the H component:

$$AE(12) = AU(12) - AL(12) \quad (2.2.1)$$

The collaboration SuperMAG, which will be explained further in section 3.2, has over 100 magnetic ground observatories at its disposal. Using magnetic data from all stations in the SuperMAG network Newell and Gjerloev 2011 used the term SME for $AE(100)$, where 100 indicates the more than 100 ground stations in SuperMAG, and the same term will be used in this thesis.

AE and SME are *local* scalar values that by using stations from various locations all over the world seek to provide a global coverage. SME differs from AE mainly by the number of ground stations used. For the development of the SME index, the coordinates were firstly transformed into a coordinate system with the horizontal component pointing towards the magnetic north. SME is then be found by taking the difference between the SMU , which is found by the station with the largest H value, and the SML , which is the station with the lowest H contribution [Newell and Gjerloev 2011]:

$$SME = SMU - SML \quad (2.2.2)$$

This procedure is a way of removing a baseline from the measurements, which is a crucial step in processing magnetic ground data. It can be done in several ways also manually by observing a nearby *quiet* day and using this as a baseline. However, SuperMAG requires an automated procedure for baseline determination hence a manually selection cannot be used here.

SME has shown high correlations with auroral power, much better than any other indices including K_p (the planetary range index) [Newell and Gjerloev 2011]. SME shows particularly good correlations with nightside auroral power [Newell and Gjerloev 2011]. This led Newell and Gjerloev 2011 to conclude that the SME represents the nightside integrated auroral power.

SML-index

A substorm is characterised as a sharp peak in auroral power, also seen as a decrease in the horizontal magnetic field component H , that lasts for about 20 min [Newell and Gjerloev 2011]. This thesis uses the following substorm identification scheme proposed by Newell

and Gjerloev 2011. A substorm onset was detected at time t_0 when the following criteria were fulfilled:

$$\begin{aligned} SML(t_0 + 1) - SML(t_0) &< -15 \text{ nT} \\ SML(t_0 + 2) - SML(t_0) &< -30 \text{ nT} \\ SML(t_0 + 3) - SML(t_0) &< -45 \text{ nT} \\ \sum_{i=4}^{i=30} \frac{SML(t_0 + i)}{26} - SML(t_0) &< -100 \text{ nT} \end{aligned}$$

The SML data are sampled every 60s (1 per min) in a 30 min buffer. From the criteria it appears that the drop in SML must be sharp, around 45nT in 3min. The drop must also be sustained, as expressed in the last criterion, for at least 30min [Newell and Gjerloev 2011]. If an onset has been identified the algorithm by Newell and Gjerloev 2011 will advance 20 min which is the minimum time interval between two onsets, however most onsets happens with larger time-span between each other.

2.3 Representing the ionospheric current system

Section 2.1 and 2.2 described our present knowledge concerning different sources of the Earth's magnetic field. In this section I will describe the physics and mathematics of the phenomena and I will introduce the modelling scheme used, in this thesis, to derive the models of the ionospheric currents during geomagnetically disturbed times.

2.3.1 Apex coordinate systems

In this thesis the magnetic apex coordinate system is used to represent the magnetic field. Richmond 1995 came up with two magnetic apex coordinate systems, the first called modified apex denoted MA and the second one called the quasi-dipole coordinate system denoted QD. A combination of these two apex coordinate systems is used in this thesis. These systems involve non-orthogonal angular coordinates established in terms of the field line apex which is defined as the highest point above the ellipsoid of the adjacent International Geomagnetic Reference Field (IGRF) magnetic field line. In magnetic apex (MA) coordinates, the latitude is defined as:

$$\lambda_m = \pm \cos^{-1} \sqrt{\frac{a + h_R}{a + h_A}} \quad (2.3.1)$$

where a is the mean radius of the Earth, h_R is a fixed reference height, and h_A is the geodetic height of the field line apex. In QD-coordinates the latitude is given by:

$$\lambda_q = \pm \cos^{-1} \sqrt{\frac{a + h}{a + h_A}} \quad (2.3.2)$$

where h is the altitude from the Earth's surface to the point of the measurement. The longitude, denoted ϕ , for both coordinate system is the centered dipole longitude of the apex. MA latitude is constant along the field lines because it only depends on h_A , while the QD-latitude is dependent on h as well hence QD-latitude is not constant along the field lines. Richmond 1995 found that magnetic Apex and Quasi-dipole coordinates were very efficient for representing FACs and horizontal sheet currents respectively, since these current systems are organized by the internal geomagnetic field.

2.3.2 The geomagnetic elements

Earth's magnetic field is described by a three-dimensional vector field known as the magnetic flux density often simply called the magnetic field \mathbf{B} . The magnetic field can be completely described by three independent elements: (X, Y, Z) , (H, D, F) , and (Z, H, D) . Where the component X is pointing towards geographic North, Y is pointing towards geographic East, and the Z component is pointing vertically down, see figure 2.6. H is known as the horizontal magnetic field intensity, D is the angle between the magnetic vector in the horizontal plane and the geographic North, known as the *declination*, F is the magnetic field intensity also known as the field strength. The *inclination* I is the angle between the horizon and the magnetic field lines. The geomagnetic elements are related in the following way:

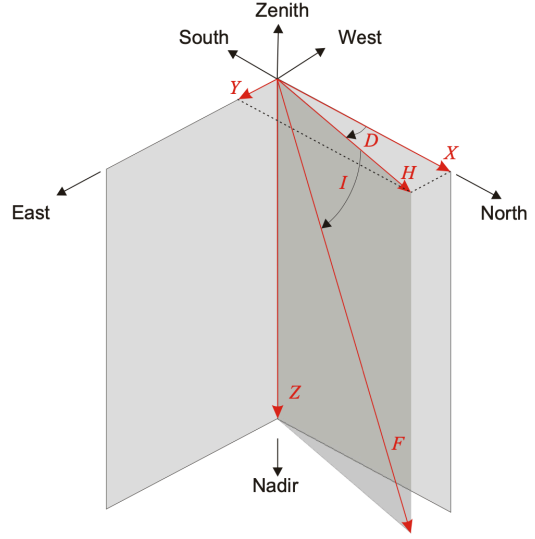


Figure 2.6: Geomagnetic elements definitions (reprinted from “Lecture notes, MSc Geomagnetism course, DTU” 2021).

$$H = \sqrt{X^2 + Y^2}$$

$$D = \tan^{-1} \left(\frac{Y}{X} \right)$$

$$X = H \cos(D)$$

$$Z = F \sin(I) = H \tan(I)$$

$$F = \sqrt{X^2 + Y^2 + Z^2}$$

$$I = \tan^{-1} \left(\frac{Z}{H} \right)$$

$$Y = H \sin(D)$$

2.3.3 Maxwell's equations

Maxwell's equations ties the magnetic field \mathbf{B} to the electric field \mathbf{E} . In vacuum the following is defined:

Faraday's law of induction:

$$\nabla \times \mathbf{E} = -\frac{\partial \mathbf{B}}{\partial t}$$

Ampere's law:

$$\nabla \times \mathbf{B} = \mu_0 \mathbf{J} + \mu_0 \epsilon_0 \frac{\partial \mathbf{E}}{\partial t}$$

Gauss law of electrostatics:

$$\nabla \cdot \mathbf{E} = \frac{\rho}{\epsilon_0}$$

Divergence free condition:

$$\nabla \cdot \mathbf{B} = 0$$

where μ_0 is a constant ($4\pi \cdot 10^{-7} [\text{Vs}/\text{Am}]$) known as the magnetic permeability of the vacuum, \mathbf{J} is the electric current density in the units of $[\text{A}/\text{m}^2]$, ϵ_0 a constant ($8.8541878176 \cdot 10^{-12} [\text{As}/\text{Vm}]$) known as the vacuum permittivity, and ρ is the density of electric charges given in units of $[\text{As}/\text{m}^3]$.

In the case of sufficiently slowly changing fields, which it is valid when investigating the magnetic field of Earth over periods longer than a few seconds, the displacement currents can be neglected such that the pre-Maxwell equations are obtained:

$$\begin{aligned}\nabla \times \mathbf{B} &= \mu_0 \mathbf{J} \\ \nabla \cdot \mathbf{J} &= 0\end{aligned}$$

In source-free regions ($\mathbf{J} = \mathbf{0}$), such as the Earth's lower atmosphere, \mathbf{B} is curl-free. This means that \mathbf{B} can be represented by the negative gradient of the scalar potential V , because \mathbf{B} is now a Laplacian potential field:

$$\mathbf{B} = -\nabla V \quad (2.3.5)$$

V can be expanded as a series of spherical harmonics (SH), which are solutions to Laplace's equation $\nabla^2 V = 0$. The above equation is only true for source-free regions hence not for altitudes above 110km. At higher altitudes the ionospheric field is, in this thesis, instead described as a sum of scalar potentials representing the *toroidal* and *poloidal* magnetic components, the next section will present this approach.

2.3.4 Modelling the ionospheric magnetic field: AMPS

In this thesis I base the modelling of the ionospheric currents, during disturbed times, on the Average Magnetic field and Polar current System (AMPS) modelling scheme (Laundal 2018). AMPS is a recent model that describes the average ionospheric magnetic field and current system for given input values of the solar wind speed, orientation of the Earth's magnetic dipole axis, magnetic field vector and the values of a solar flux index $F_{10.7}$ [Laundal 2018]. AMPS was constructed using measurements from the satellites CHAMP and Swarm where the core field and magnetic field produced by large-scale magnetospheric currents, as estimated using the CHAOS field model (Olsen, Lühr, et al. 2014, Finlay et al. 2020), have been removed. The remaining signals are assumed to be the magnetic field associated with the ionospheric currents. Model parameters are estimated from millions of measurements in order to produce a model of the ionospheric field that can be evaluated at an location and time of interest, given the specified input values. This model is an improvement over previous models in that it accounts for the time-dependent core field and the large-scale magnetospheric field. An advantage of the AMPS model is that it is capable of making precise comparisons between the northern and southern hemisphere and it describes the total ionospheric field including both FACs and the horizontal currents. Thus no assumptions about the conductivity in the ionosphere are needed when deriving the currents [Laundal 2018]. The software for evaluating AMPS is freely available to the scientific community as a Swarm data product and its software is written in the programming language Python. The following paragraphs will present the mathematical building blocks of the AMPS, and this thesis', modelling scheme.

As mentioned V can be expanded as a series of SH however, due to the presence of currents in the ionosphere we cannot represent the magnetic field as a purely Laplacian potential. It is instead represented as a sum of two scalar potentials T and P that represents the *toroidal* and *poloidal* components respectively:

$$\mathbf{B}^{ion} = \mathbf{B}^{pol} + \mathbf{B}^{tor} = \nabla \times \nabla \times \mathbf{r}P + \mathbf{r} \times \nabla T \quad (2.3.6)$$

Equation 2.3.6 expresses that the magnetic field perturbation, associated with ionospheric currents, \mathbf{B}^{ion} is a combination of the poloidal perturbation \mathbf{B}^{pol} and the toroidal perturbation \mathbf{B}^{tor} , where \mathbf{r} is a unit vector. The poloidal field is essentially a Laplacian field due

to the fact that \mathbf{B}^{ion} is sampled in a thin spherical shell compared to the radius. Equation 2.3.6 can thus be rewritten as:

$$\mathbf{B}^{ion} = \mathbf{B}^{pol} + \mathbf{B}^{tor} = -\nabla V - \mathbf{r} \times \nabla T = -\nabla V + \nabla \times T\mathbf{r} \quad (2.3.7)$$

∇V represents the magnetic field produced by ionospheric currents that are internal to the shell at where the satellite orbits e.g. DFCs since these consist of purely toroidal currents that will create a poloidal field. The other part of equation 2.3.7, the toroidal magnetic field, is associated with the radial currents that cross the shell e.g. FACs consisting of poloidal currents that produce a toroidal field; the resulting magnetic fields produced purely by the FACs is:

$$\mathbf{B}^{tor} = \nabla \times T\mathbf{r} = -\mathbf{r} \times \nabla T \quad (2.3.8)$$

In this thesis, it will be assumed that after removal of a reference field model that includes core, lithospheric and magnetospheric sources, such as the CHAOS field model [Olsen, Lühr, et al. 2014], the remainder, \mathbf{B}^{ion} , is due to currents produced by the ionosphere as well as un-modelled induced currents on ground [Laundal, Finlay, and Olsen 2016].

The potentials V and T can be expanded in a basis of spherical harmonics as done in Laundal, Finlay, Olsen, and Reistad 2018 in apex coordinates:

$$T(\lambda_m, \phi_{MLT}) = \sum_{n,m} P_n^m(\sin \lambda_m) [\psi_n^m \cos(m\phi_{MLT}) + \eta_n^m \sin(m\phi_{MLT})] \quad (2.3.9)$$

$$V(\lambda_q, \phi_{MLT}, h) = a \sum_{n,m} \left(\frac{a}{a+h} \right)^{n+1} P_n^m(\sin \lambda_q) [g_n^m \cos(m\phi_{MLT}) + h_n^m \sin(m\phi_{MLT})] \quad (2.3.10)$$

where $(\psi_n^m, \eta_n^m, g_n^m, h_n^m)$ are the spherical harmonic coefficients of degree n and order m , $P_n^m(\sin \lambda_m)$ and $P_n^m(\sin \lambda_q)$ are Schmidt semi-normalised associated Legendre functions, and ϕ_{MLT} is the magnetic local time that replaces the apex longitude. This replacement can be done because the magnetic disturbances, in the ionosphere, mainly occur from interactions with the solar wind and are better organized with respect to the sun's position, rather than an Earth-fixed longitude [Laundal, Finlay, and Olsen 2016]. In radians ϕ_{MLT} can be written as:

$$\phi_{MLT} = \phi - \phi_{noon} + \pi \quad (2.3.11)$$

where ϕ_{noon} is the apex longitude of the magnetic meridian. For the purpose of investigating the disturbances in the ionospheric field a noon meridian is chosen for high latitudes.

Because the FACs flow along the magnetic field lines MA coordinates are often used for toroidal field representation [Richmond 1995]. It is assumed that T is constant along the IGRF magnetic field lines and so it is possible to express equation 2.3.8 using MA coordinates for the toroidal potential ∇T [Richmond 1995]:

$$\nabla T = \frac{\mathbf{d}_1}{(a+h_R) \cos \lambda_m} \frac{\partial T}{\partial \phi_{MLT}} - \frac{\mathbf{d}_2}{(a+h_R) \sin I_m} \frac{\partial T}{\partial \lambda_m} \quad (2.3.12)$$

where \mathbf{d}_1 and \mathbf{d}_2 are MA base vectors [Richmond 1995] and $\sin I_m$ is given by:

$$\sin I_m = \frac{2 \sin \lambda_m}{\sqrt{4 - 3 \cos^2 \lambda_m}} \quad (2.3.13)$$

The related toroidal magnetic field can then be written as:

$$\mathbf{B}^{\text{tor}} = \mathbf{k} \times \left[\frac{\mathbf{d}_1}{\cos \lambda_m} \frac{\partial T}{\partial \phi} - \frac{\mathbf{d}_2}{\sin I_m} \frac{\partial T}{\partial \lambda_m} \right] \quad (2.3.14)$$

where \mathbf{k} is a unit vector relative to the ellipsoid.

When describing the poloidal field QD coordinates are used. This is the case because the poloidal potential depends on currents that are far away from the satellites and at satellite altitude these currents are mainly the horizontal currents. The horizontal currents in the ionosphere are mainly situated in the conducting E-layer [Kelley 2007] and hence to describe the radial dependence one needs a system that can include heights thus QD coordinates are used. The poloidal field can in QD-coordinates \mathbf{B}^{pol} therefore be written as [Richmond 1995]:

$$\mathbf{B}^{\text{pol}} = -\nabla V = -\frac{1}{a+h} \frac{1}{\cos \lambda_q} \frac{\partial V}{\partial \phi_{MLT}} \mathbf{f}_2 \times \mathbf{k} - \frac{1}{a+h} \frac{\partial V}{\partial \lambda_q} \mathbf{k} \times \mathbf{f}_1 - \sqrt{F_m} \frac{\partial V}{\partial h} \mathbf{k}. \quad (2.3.15)$$

where \mathbf{f}_1 and \mathbf{f}_2 are the QD base vectors and F_m is the magnitude of their cross product, $|\mathbf{f}_1 \times \mathbf{f}_2|$ [Richmond 1995].

The total field perturbation, or ionospheric magnetic field, in apex coordinates can thus be written as a combination of equation 2.3.14 and 2.3.15. Following Laundal, Finlay, and Olsen 2016 the field components in the geodetic east B_e , north B_n and up B_u directions are then respectively:

$$B_e = \frac{-d_{1,n}}{\cos \lambda_m} \frac{\partial T}{\partial \phi_{MLT}} + \frac{d_{2,n}}{\sin I_m} \frac{\partial T}{\partial \lambda_m} - \frac{f_{2,n}}{a+h} \frac{1}{\cos \lambda_q} \frac{\partial V}{\partial \phi_{MLT}} + \frac{f_{1,n}}{a+h} \frac{\partial V}{\partial \lambda_q} \quad (2.3.16)$$

$$B_n = \frac{d_{1,e}}{\cos \lambda_m} \frac{\partial T}{\partial \phi_{MLT}} - \frac{d_{2,e}}{\sin I_m} \frac{\partial T}{\partial \lambda_m} + \frac{f_{2,e}}{a+h} \frac{1}{\cos \lambda_q} \frac{\partial V}{\partial \phi_{MLT}} - \frac{f_{1,e}}{a+h} \frac{\partial V}{\partial \lambda_q} \quad (2.3.17)$$

$$B_u = -\sqrt{F_m} \frac{\partial V}{\partial h} \quad (2.3.18)$$

AMPS is a time dependent model via a number of external parameters: the IMF components $B_{\text{IMF},y}$ and $B_{\text{IMF},z}$, solar wind speed v_x , dipole tilt angle β_{tilt} , and the solar radio flux index $F_{10.7}$ [Laundal, Finlay, Olsen, and Reistad 2018]. These variables are available for the times of the input data from the satellites Swarm and CHAMP. The modelling procedure, used in this thesis, differs from the AMPS modelling; here I include the *SML* index as an additional external input for the model. For each of the spherical harmonic coefficients $(\psi_n^m, \eta_n^m, g_n^m, h_n^m)$ in equations 2.3.9 and 2.3.10 an expansion of the external parameters are made. As an example the expansion for g_n^m is given by:

$$\begin{aligned} g_n^m = & g_{n1}^m + g_{n2}^m \sin \theta_c + g_{n3}^m \cos \theta_c + g_{n4}^m \epsilon + g_{n5}^m \epsilon \sin \theta_c + g_{n6}^m \epsilon \cos \theta_c + \\ & g_{n7}^m \beta_{\text{tilt}} + g_{n8}^m \beta_{\text{tilt}} \sin \theta_c + g_{n9}^m \beta_{\text{tilt}} \cos \theta_c + g_{n10}^m \beta_{\text{tilt}} \epsilon + g_{n11}^m \beta_{\text{tilt}} \epsilon \sin \theta_c + \\ & g_{n12}^m \beta_{\text{tilt}} \epsilon \cos \theta_c + g_{n13}^m \tau + g_{n14}^m \tau \sin \theta_c + g_{n15}^m \tau \cos \theta_c + g_{n16}^m \tau \beta_{\text{tilt}} + \\ & g_{n17}^m \beta_{\text{tilt}} \tau \sin \theta_c + g_{n18}^m \beta_{\text{tilt}} \tau \cos \theta_c + g_{n19}^m F_{10.7} + g_{n20}^m SML \end{aligned} \quad (2.3.19)$$

here θ_c , in degrees, is the IMF clock angle that is given by:

$$\theta_c = \arctan 2(B_{\text{IMF},y}, B_{\text{IMF},z}) \quad (2.3.20)$$

ϵ , with units of mV/m, is the solar wind-magnetospheric coupling function expressed as:

$$\epsilon = 10^{-3}|v_x|^{\frac{4}{3}}\sqrt{B_{\text{IMF},y}^2 + B_{\text{IMF},z}^2}^{\frac{2}{3}}\sin^{\frac{8}{3}}\left(\frac{|\theta_c|}{2}\right) \quad (2.3.21)$$

The tilt angle β_{tilt} , in units of degrees, is expressed in the following way where $\mathbf{m}_{\text{dipole}}$ is the unit vector in the direction of the magnetic dipole axis and \mathbf{s} represents a unit vector pointing in the direction of the Sun:

$$\beta_{\text{tilt}} = \arcsin(\mathbf{s} \cdot \mathbf{m}_{\text{dipole}}) \quad (2.3.22)$$

τ is another solar wind-magnetospheric coupling function that deals with lobe reconnection rate on the night-side of the magnetotail. τ , with units of mV/m, is expressed as:

$$\tau = 10^{-3}|v_x|^{\frac{4}{3}}\sqrt{B_{\text{IMF},y}^2 + B_{\text{IMF},z}^2}^{\frac{2}{3}}\cos^{\frac{8}{3}}\left(\frac{\theta_c}{2}\right) \quad (2.3.23)$$

2.4 Model parameter estimation

Now that I can represent the ionospheric current system by a toroidal-poloidal decomposition I need to establish the model parameters which are the SH coefficients $(\psi_n^m, \eta_n^m, g_n^m, h_n^m)$. To solve for the model parameters I utilise the robust regularised least squares method presented in this section.

The total magnetic field of Earth can be approximated as:

$$\mathbf{B} = \mathbf{B}^{\text{INT}} + \mathbf{B}^{\text{mag}} + \mathbf{B}^{\text{ion}} \quad (2.4.1)$$

Here \mathbf{B}^{INT} represents the magnetic field caused by the internal parts, \mathbf{B}^{mag} is the magnetic field caused by the magnetosphere, and \mathbf{B}^{ion} is the ionospheric magnetic field. In this thesis the field of interest is \mathbf{B}^{ion} and thus we would like to construct a model of this field based on the observed values. This is done by solving an inverse problem by means of robust regularised least squares.

A linear forward problem, where \mathbf{d} is a vector containing the data, \mathbf{G} is a design matrix, and \mathbf{m} is a vector containing the model parameters, can be written as:

$$\mathbf{d} = \mathbf{G}\mathbf{m} \quad (2.4.2)$$

The data vector \mathbf{d} has the size N which is the number of data points, \mathbf{m} has the size M which is the number of model parameter which means that the matrix \mathbf{G} , connecting the model and the data, has a size of $N \times M$. In order to solve for the model parameters in \mathbf{m} the following loss function is minimised:

$$\Phi(\mathbf{m}) = \frac{1}{2}(\mathbf{d} - \mathbf{G}\mathbf{m})^T \mathbf{W}(\mathbf{d} - \mathbf{G}\mathbf{m}) + \frac{1}{2}\mathbf{m}^T \mathbf{\Lambda} \mathbf{m} \quad (2.4.3)$$

Here $\mathbf{\Lambda}$ is the regularisation matrix of size $M \times M$ where α^2 is a regularization parameter, and \mathbf{W} is the diagonal weight matrix containing Huber weights. The diagonal weight matrix is given by:

$$\mathbf{W} = \mathbf{w}_{\text{huber}} \mathbf{C}_d^{-1} \quad (2.4.4)$$

where \mathbf{C}_d is the data covariance matrix and \mathbf{w}_{huber} denotes the Huber weights vector updated in every iteration; each element of \mathbf{w}_{huber} is computed in the following way where c is the tuning constant:

$$w_{huber,i} = \begin{cases} \frac{c}{e_i} & e_i > c \\ 1 & |e_i| \leq c \\ -\frac{c}{e_i} & e_i < -c \end{cases} \quad (2.4.5)$$

e_i denotes the individual residuals for each data point, where σ is the expected data error:

$$e_i = \frac{d_i - (\mathbf{G}\mathbf{m})_i}{\sigma} \quad (2.4.6)$$

The data covariance matrix \mathbf{C}_d is given by:

$$\mathbf{C}_d = \sigma^2 \mathbf{I}_d \quad (2.4.7)$$

here \mathbf{I}_d is the identity matrix and σ is the a-priori data error. The regularisation matrix $\mathbf{\Lambda}$ is given by:

$$\mathbf{\Lambda} = \alpha^2 \mathbf{C}_m^{-1} \quad (2.4.8)$$

where \mathbf{C}_m is the model covariance matrix given by:

$$\mathbf{C}_m = \mathbf{G}^{-g} \mathbf{C}_d (\mathbf{G}^{-g})^T \quad (2.4.9)$$

where \mathbf{G}^{-g} denotes:

$$\mathbf{G}^{-g} = (\mathbf{G}^T \mathbf{G} + \alpha^2 \mathbf{I}_d)^{-1} \mathbf{G}^T \quad (2.4.10)$$

A solution that minimises the loss function can be obtained by taking the derivative with respect to the model parameters:

$$\frac{\partial \Phi}{\partial \mathbf{m}} = \mathbf{G}^T \mathbf{W}(\mathbf{d} - \mathbf{G}\mathbf{m}) + \mathbf{\Lambda}\mathbf{m} \quad (2.4.11)$$

By setting equation 2.4.11 to zero the solution for the model parameters is obtained:

$$\mathbf{m} = (\mathbf{G}^T \mathbf{W} \mathbf{G} + \mathbf{\Lambda})^{-1} \mathbf{G}^T \mathbf{d} \quad (2.4.12)$$

The solution is found through an iterative process because the Huber weights depend on the residuals hence they need to be updated after each iteration.

In chapter 4 I will present specific output statistics of the model including normalised misfit ($misfit_{norm}$) and model norm ($model_{norm}$) these parameters are computed in the following way:

$$misfit_{norm} = \frac{\mathbf{e}^T \mathbf{W} \mathbf{e}}{N} \quad model_{norm} = \mathbf{m}^T \mathbf{\Lambda} \mathbf{m} \quad (2.4.13)$$

2.4.1 Multifit

The ionospheric currents modelling of this thesis is carried out by using the Python package *Multifit* developed by Dr. Clemens Kloss at DTU Space. Multifit consist of the field modelling methods AMPS and *CHAOS*. *CHAOS* is, much like AMPS, a time-dependent high-resolution modelling procedure that estimates the spherical harmonic coefficients for both internal and external fields [Finlay et al. 2020].

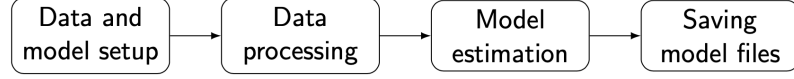


Figure 2.7: The figure displays the four different parts/processes in the driver.py script (reprinted from Kloss 2021).

To utilise Multifit a driver script is created. The driver script is called "driver.py" and it contains all the information and inputs Multifit needs in order to produce climatological models. Figure 2.7 illustrates schematically the different parts in driver.py. The first part of driver.py contains information about directories of the Swarm data and which variables to include as well as the a-priori data error σ . The second part process the data using the specifications given in the first part.

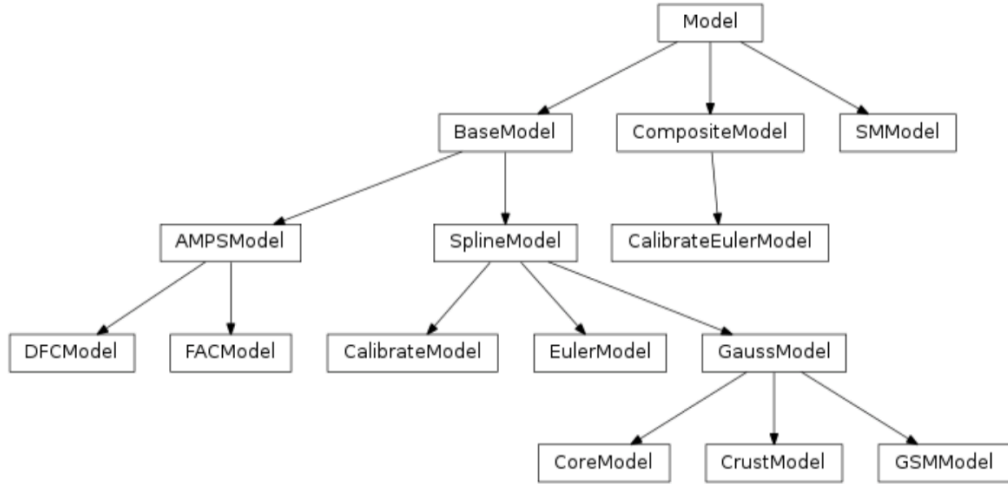


Figure 2.8: A schematic illustration of the different models produced by driver.py (reprinted from Kloss 2021).

The third part of driver.py contains information about the computation scheme. Here the user can specify the solution approach, e.g. least squares (LS) or Tikhonov, and the truncation degree and order. In this thesis Multifit is set to run 10 iterations for a model where the first iteration always uses LS and the remaining 9 iterations uses a robust regularisation with Huber-weighting. The last part of driver.py saves the model parameter estimates and in the specified directory. The models that are created can be seen in figure 2.8.

Observations

3.1 Swarm data

On the 22nd of November 2013 the European Space Agency (ESA) launched a satellite mission called Swarm. Swarm is a constellation consisting of three satellites Swarm A, Swarm B, and Swarm C. Swarm A and C are flying side-by-side at an altitude of 450km while Swarm B is flying at an altitude of 530km [ESA Swarm mission: An overview 2021]. The satellites are polar-orbiting which allows for a global coverage with the exception of a small polar-gap. The satellites measure the Earth's magnetic field strength and direction.

The 9 meter long satellites have a 4 meter long boom where the magnetometers are located - strategically placed away from electronics on board the spacecraft. There are two kinds of magnetometers on board, a vector magnetometer (VFM) measuring the direction of the magnetic field using a three-axis fluxgate along with star trackers, and a scalar magnetometer (ASM) that measures the strength of the magnetic field. The star trackers (STR), determine the altitude of the spacecraft. Figure 3.1 shows a side-view of the Swarm satellites with locations of the instruments shown.

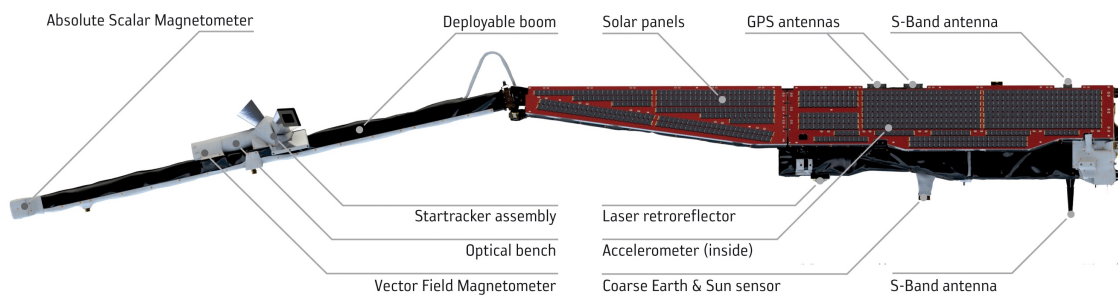


Figure 3.1: Instruments on board the Swarm mission, reprinted from *Swarm instruments* 2012.

In this thesis the climatological models of ionospheric currents, with a focus on disturbed times, are developed using magnetic field measurements from the Swarm mission. The datafiles are obtained through ESA¹. An example of a datafile extracted from ESA is SW_OPER_MAGA_LR_1B_20140201T000000_20140201T235959_0601_MDR_MAG_LR.cdf where the number 0601 refers to the baseline. Data from the years 2014-2017

¹<https://swarm-diss.eo.esa.int>

from Swarm A is utilised. The data is extracted from .cdf files that have a sampling rate of 1 measurement per second.

Based on the raw Swarm L1b .cdf files a datafile, containing all measurements from 01/01/2014 to 31/12/2017 along with auxiliary data from <https://omniweb.gsfc.nasa.gov/ow.html>, was created. The content of this datafile can be seen in table 3.1. This file, is further processed before it is used as an input for the ionospheric field modelling. The further processing will be described in section 3.3.

Variable	Size	Description
\mathbf{B}_{NEC}	$3 \times N$	Magnetic field vector in Earth centered coordinates
θ_c	N	Clock angle in degrees
ϵ	N	Solar wind magnetospheric coupling function
$F_{10.7}$	N	Solar radio flux index measured in sfu
$B_{IMF,y}$	N	IMF component in the y-direction
$B_{IMF,z}$	N	IMF component in the x-direction
λ_m	N	Modified-Apex latitude
MLT	N	Magnetic local time in degrees
ϕ	N	Longitude in degrees
λ_q	N	Latitude in QD coordinates
R	N	(Radius) Distance from satellite to center of the Earth in km
RC_e	N	External RC-index
RC_i	N	Internal RC-index
σ	N	Standard deviation in nT or data error
SML	N	SuperMAG version of the AL index
τ	N	Solar wind-magnetospheric coupling function that deals with lobe reconnection rate on the night-side of the magnetotail
θ	N	Co-latitude in degrees.
Time	N	Time in Modified Julian Date 2000 (MDJ2000)
β_{tilt}	N	Dipole tilt angle in degrees
v_x	N	Solar wind speed in km/s

Table 3.1: The content and dimensions of the variables in the datafile where N is the number of data points.

In figure 3.2 are shown an example of the three components in \mathbf{B}_{NEC} where the internal and magnetospheric field is subtracted from the measurements of Swarm A. This specific event will be investigated in the upcoming chapters.

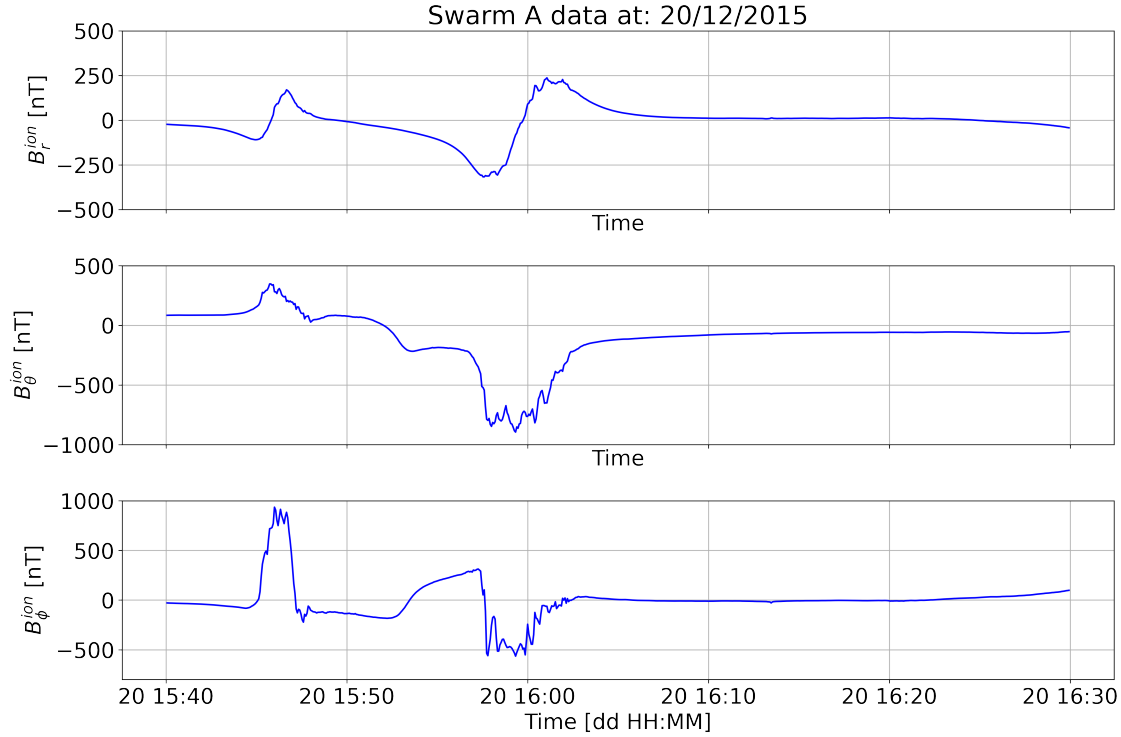


Figure 3.2: An example of Swarm A data, where the internal and magnetospheric field is subtracted, taken at 20/12/2015 during a large substorm that started at 15:40 UTC.

3.2 Ground stations and observatories

INTERMAGNET, short for *International Real-time Magnetic Observatory Network*, is an organisation that since 1991 has operated a global network of more than 100 geomagnetic observatories. The data, at the ground observatories, is measured by fluxgate magnetometers. The magnetometers measure the variation of the vector geomagnetic field in three directions. The measurements are calibrated using measurements of D , I , measured by a non-magnetic theodolite and a single axis fluxgate sensor, and absolute measurements of F by the use of a proton precession-type scalar magnetometer.

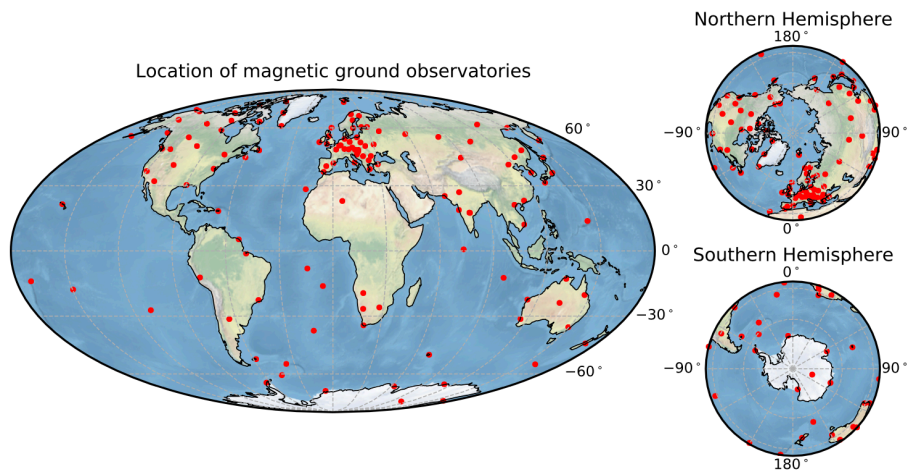


Figure 3.3: A map of the locations of 127 ground observatories that are currently a part of the INTERMAGNET collaboration.

Figure 3.3 shows the location of 127 magnetic observatories that are a part of INTERMAGNET. Most stations are located in the northern hemisphere, mainly in Europe, the uneven distribution means that it is not possible to achieve proper global coverage. This is why LEO satellites play such an important role in studies of Earth’s magnetic field. Nonetheless, ground observatories have several advantages: (1) they provide continuous monitoring and high quality data at fixed locations that allows for investigation of the past and present changes in the magnetic field (2) the stations are located at the Earth’s surface i.e. between two magnetic sources which could be important for future separation of sources, (3) their magnetic data allows for derivation of magnetic activity indices e.g. Kp , Dst , AL and AU [Kauristie et al. 2017]. The magnetic activity indices play an important part of the selection of magnetic disturbed times that will be carried out in this thesis.

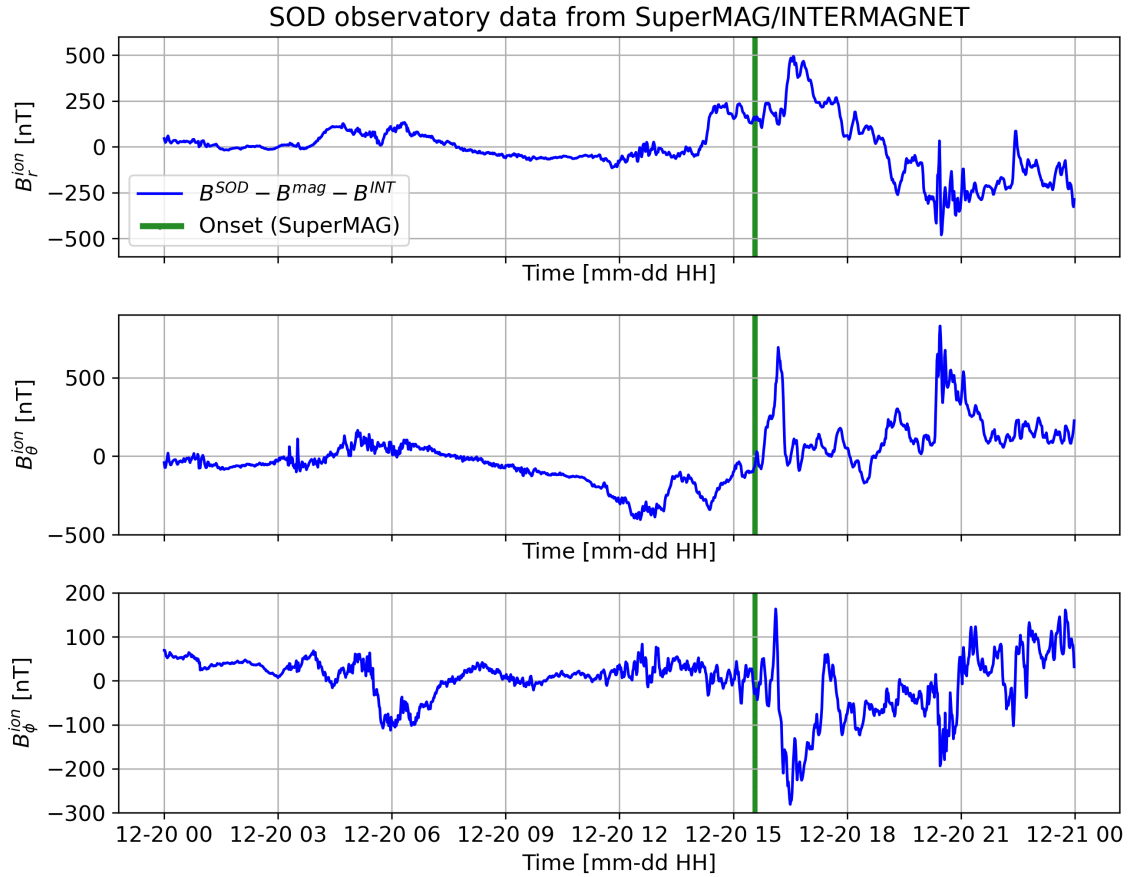


Figure 3.4: An example of ground observatory data obtained from INTERMAGNET during a substorm at 20/12/2015, at the station SOD in Finland. The internal and magnetospheric field have been subtracted from the observatory data B^{SOD} . The vertical green line represents the onset of the substorm found by SuperMAG.

SuperMAG is a collaboration between different organisations worldwide that conduct measurements and process magnetic 3D vector data from more than 300 ground based magnetometers [SuperMAG 2021]. The data is a combination of absolute measurements, carried out by INTERMAGNET observatories, and relative (variometer) measurements. SuperMAG provides data with or without a subtraction of baseline. All data has been resampled to 1 min temporal resolution and all units have been converted to nano Tesla [Newell and Gjerloev 2011]. SuperMAG provides a magnetic activity index called the *SuperMAG elec-*

trojet index SME which is utilised in this thesis, more information is provided in section 2.2.2 and 2.2.2.

A second type of data product from SuperMAG is also used in this thesis. This type is a substorm list which is obtained from the SuperMAG's website². This substorm list includes magnetic longitude, latitude, MLT, and date/time given in UTC of each recorded onset of a substorm according to Newell and Gjerloev 2011. It was used here to validate my data selection scheme by comparing the SuperMAG substorms to the data selected here, further details of the method are given in section 2.2.2.

In figure 3.4 is shown an example of ground station data from the observatory SOD in Finland. B_r^{ion} , B_θ^{ion} , and B_ϕ^{ion} represent the three components of the ionospheric field which are found by subtracting the internal B^{INT} and magnetospheric B^{mag} field from the observatory data B^{SOD} . This specific observatory data and substorm event will be used in the later chapters as a part of the assessment of the produced models.

3.3 Data selection

The datafile, collecting the Swarm data and auxiliary information from 2014 to 2017, contains data from both magnetically disturbed and quiet times. Since the focus of this thesis is on substorm activity a data selection scheme was devised that selects magnetically disturbed times. This selection scheme will be introduced in the following sections.

3.3.1 Selection of disturbed conditions using *SML* index

This algorithm has, in this thesis, been implemented in the Python programming language and applied to the datafile, see appendix B for information about the script. The algorithm detected 7775 substorm onsets between 2014 and 2017 while the official substorm list, provided by SuperMAG, detected 7270 substorm onsets. Figure 3.5 shows a plot of the *SML* indices for the period 2015-02-25 to 2015-03-01. The red dots represents the time and *SML* value of the onsets determined by the implemented algorithm and the Newell and Gjerloev list. The green vertical lines display the time of the onsets determined by ground stations (the substorm list) produced by the SuperMAG community. The figure shows that the determined onsets based on Swarm data times, coincide well with the onsets found by SuperMAG with very few exceptions.

After establishing the onsets of the substorms we wish to go further and to select all data within a substorm and this is done by imposing a *substorm criteria*. I define a *change limit* ($dSML_{limit}$) as the the minimum absolute change in *SML* before the data can be classified as being *quiet*. The change limit is set to 0.75nT/sec which has been chosen so that there is still a sufficient amount of data to provide a global coverage but ensuring that the main part of the data selected is indeed linked to substorm activity. I also define a *quiet limit*, denoted t_{ql} , which specifies how long time a time interval is considered in order to assess whether the data is classified as being *quiet*. The quiet limit is set to 15min based on the same logic as for the choice of change limit.

²<https://supermag.jhuapl.edu/substorms/?start=2014-01-01T00%3A00%3A00.000Z&interval=35040%3A00&fidelity=low>

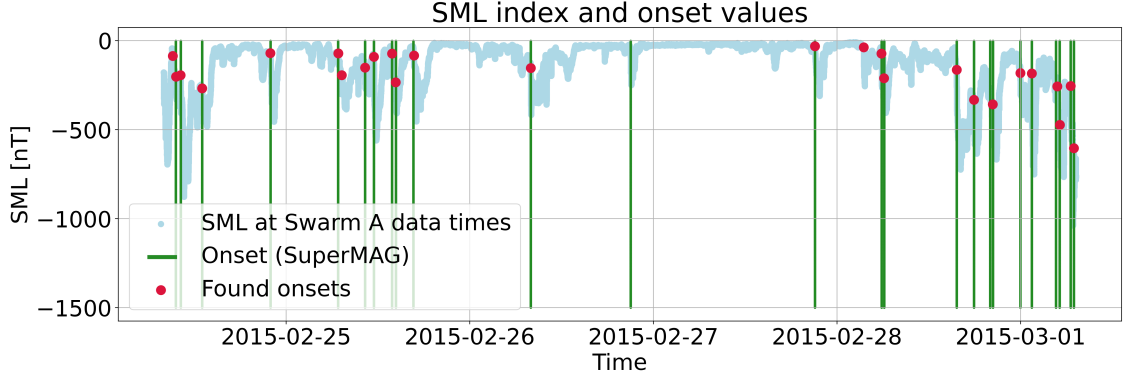


Figure 3.5: A timeseries of SML indices in the end of February to the beginning of March 2015. The red dots represents the onsets found using SML data interpolated to the times of Swarm A data while the vertical green lines represents onset-times determined directly by SuperMAG.

The absolute change in SML is given by:

$$dSML_{abs} = \left| \frac{dSML}{dt} \right| \quad (3.3.1)$$

A set of data points (from an onset t_0 to $t_0 + t_{ql}$) is classified as disturbed data when the following is satisfied:

$$\frac{1}{n_t} \sum_{i=t_0}^{t_0+t_{ql}} dSML_{abs}(i) > dSML_{limit} \quad (3.3.2)$$

where n_t is the number of data points in the time interval from t_0 to $t_0 + t_{ql}$. Equation 3.3.2 is implemented in a Python script that runs through every detected substorm onset (see appendix B for information about the script). All data points after an onset that fulfil this criteria are selected as disturbed time data and are collected in a file named SwarmA_disturbed_dSML.h5.

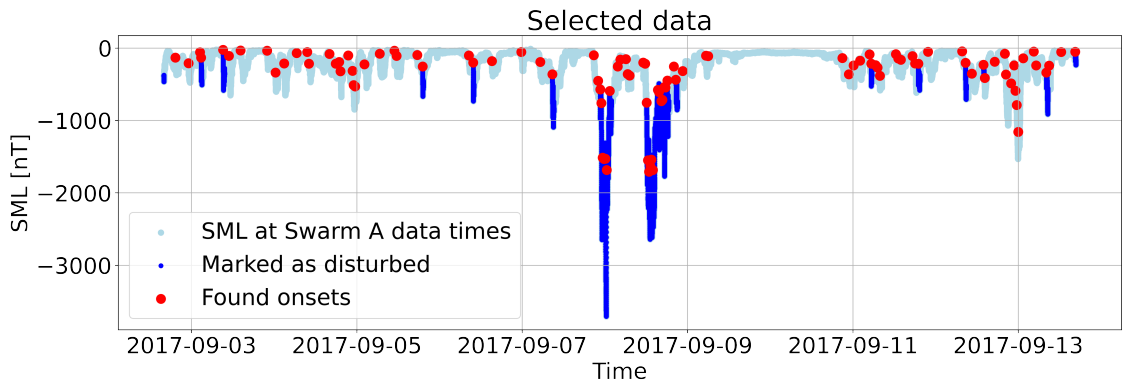


Figure 3.6: A timeseries of SML indices for Swarm A data times for 03/09/2015 - 13/09/2015. The red dots represents the onsets found using the algorithm described above while the dark-blue dots denotes the selected disturbed data.

Figure 3.6 shows an example of SML indices at times of Swarm A data and which points the above algorithm selects as disturbed times for the 10 day period 2017-09-03 to 2017-09-13. Figure 3.6 shows examples of both small and large substorms. It shows that not all small substorm-type dips in the SML index get selected because they do not fulfil the criteria within the chosen $dSML_{limit}$ and t_{ql} . This selection can be tuned by changing these constants, however here it is preferred to choose only disturbed times with as little as possible contamination of quiet times.

The resulting datafile of Swarm A measurements during disturbed substorm-related times, `SwarmA_disturbed_cleaned_dSML.h5`, is then cleaned for NaN-values and large outliers ready for use in the modelling process. Figure 3.7 displays the distribution of SML indices for the cleaned datafile and the original datafile called `Multifit_datafile.h5`. The figure are showing that the selection scheme has, as desired, mainly chosen data points with high SML values. The histograms also show a major reduction in data points, in fact the total number of datapoints in the cleaned datafile is $N = 501345$ thus only about 1.59% of the original dataset is kept.

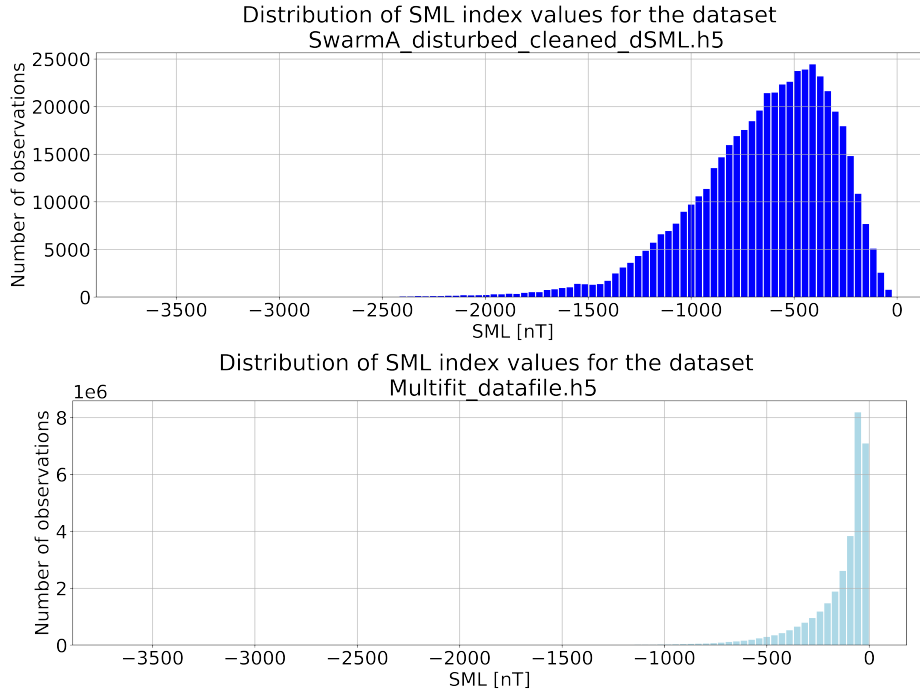


Figure 3.7: The two figures show the distribution of SML indices for `SwarmA_disturbed_cleaned_dSML.h5` (top) and the original un-selected `Multifit_datafile.h5` (bottom).

The content of the final selected and cleaned Swarm A dataset is listed in table 3.1 and figure 3.9 shows the related distribution of the most important input variables for the ionospheric modelling process. Table 3.2 displays the value at the mode of the histograms for the variables. Figure 3.8 shows two density plots with corresponding histograms of the IMF solar wind speed v_x vs. the IMF magnetic field strength B_{IMF} (figure 3.8a) and the IMF components B_z and B_y (figure 3.8b). Figure 3.8a shows that the main part of B_{IMF} has a value of 0-10nT while the solar wind speed is mainly from 600-700km/s.

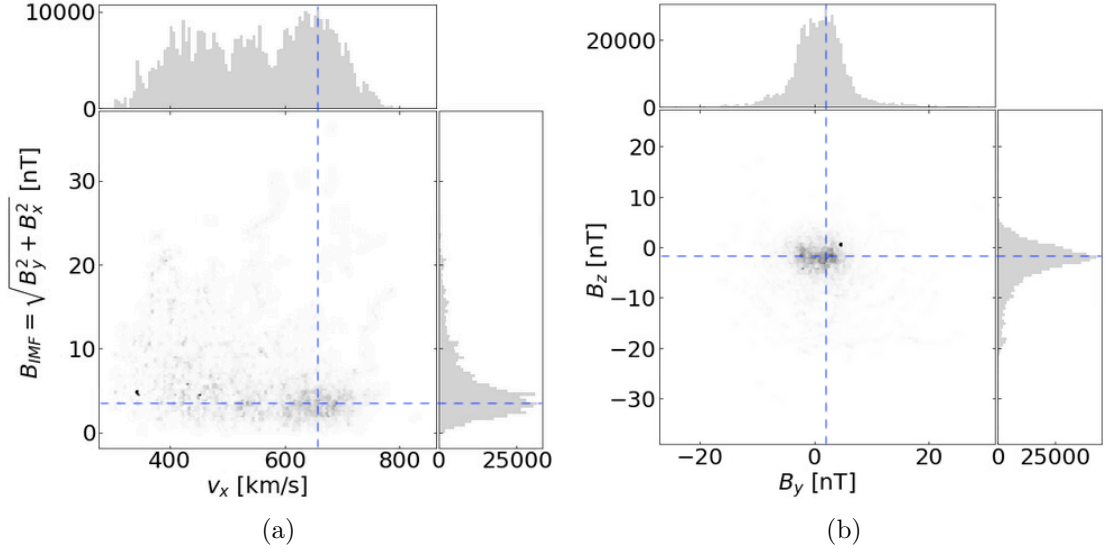


Figure 3.8: Two density plots displaying the relationship between the solar wind speed v_x and the IMF magnetic field strength B (3.8a) and between the two different components of the IMF B_z and B_y (3.8b). The dashed blue lines represents the mode of the distributions.

The histogram containing the distribution of QD-latitude in figure 3.9 shows that despite the reduction in data points a satisfactory global coverage is still achieved in the dataset SwarmA_disturbed_cleaned_dSML.h5. There is a gap in the distribution of MA-latitude around 0 degrees. This is expected and due to the way the MA-coordinates system is constructed and not caused by the reduction in data. Dealing with this data distribution requires regularisation of the FAC part of the model (see appendix A.1).

The histogram of clock angles shows that the data distribution is slightly biased towards clock angles of 90° to 180° . This is a consequence of the *SML* selection.

Variable	Mode of distribution
SML	-428.35 nT
v_x	655.24 km/s
B_{IMF}	3.30 nT
$B_{IMF,y}$	1.77 nT
$B_{IMF,z}$	-2.23 nT
F10.7	71.23 sfu
Tilt angle β_{tilt}	-13.92°
Clock angle θ_c	118.31°

Table 3.2: The value of the each variable at the mode of the histograms are shown in the table. These values will be referred to as "typical conditions" throughout this thesis.

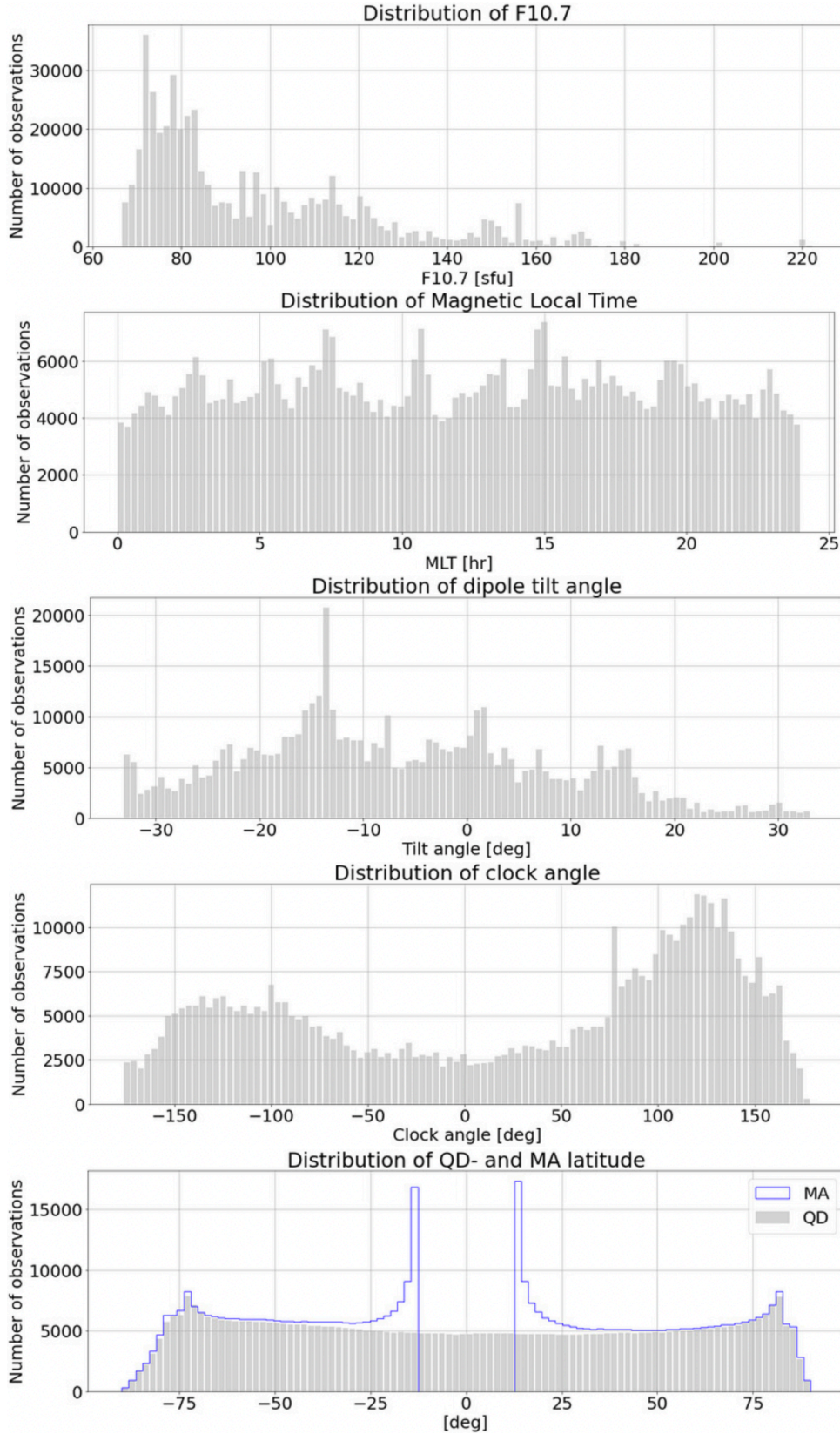


Figure 3.9: Histograms showing the distribution of data points in the processed datafile SwarmA_disturbed_cleaned_dSML.h5.

Results

The aim of this thesis is to derive a climatological model of the ionospheric currents for magnetic disturbed times. We begin by presenting an example model (Model A) obtained by the methods presented in the previous chapters. The model setup, fit to the contributing data, and typical ionospheric currents during disturbed conditions, are documented in section 4.1. In section 4.2 the fit to the collected data during two example substorms, and associated dynamics of the current system are presented. Comparison between the model and independent ground and satellite data will be presented in section 4.3. Finally, results from a model derived using an alternative dataset, referred to as Model B, will be presented in section 4.4.

4.1 A model of the polar ionospheric field during disturbed conditions

4.1.1 Model setup

The climatological model of the ionospheric field, developed in this thesis, is created by using the specifications listed in table 4.1. The specifications were determined by running a series of test models for the regularisation parameter α^2 for the FAC, the a-priori data error σ , the truncation levels, and convergence level. These test models are documented in appendix A.

	Reg. parameter α^2	Total number of iterations	Data error σ	Truncation level m_{DFC}	Truncation level m_{FAC}	Truncation level n_{DFC}	Truncation level n_{FAC}
Model A & B	$1e6 \text{ nT}^{-2}$	10	40nT	3	3	45	65

Table 4.1: Displayed are the chosen α^2 , max. iteration, σ , and truncation levels that are used to produce Model A.

4.1.2 Fit of model to Swarm data

In this subsection the fit of Model A to the contributing Swarm data is presented. The summary statistics is documented alongside with histograms of the residuals and how they are distributed with position versus QD-latitude and MLT.

Table 4.2 displays the summary misfit statistics for the fit of the modelled ionospheric field to the Swarm magnetic field measurements considering the three components separately. The third column contains the RMS of the un-weighted residuals for each ionospheric component. The RMS of B_θ^{ion} and B_ϕ^{ion} are larger than the RMS of B_r^{ion} both in the weighted and in the un-weighted case. This implies that we are not able to fit B_θ^{ion} and B_ϕ^{ion} as accurately as B_r^{ion} .

When applying the Huber weights to the data the RMS significantly changes as seen in column five. This means that the Huber weights indeed affect the modelling of the ionospheric field. However the mean of the Huber weights, seen in column six, are reasonably close to 1 which means that only a small percentage of data points are down-weighted. This is consistent with the histograms of residuals, figure 4.2, which show a small number of very large outliers.

Model A	Mean of residuals (nT)	RMS (nT)	Mean of weighted residuals (nT)	Weighted RMS (nT)	Mean of Huber weights
B_r^{ion}	-0.6245	31.6950	0.1923	14.9891	0.9811
B_θ^{ion}	3.4703	75.6737	3.2916	27.3335	0.9317
B_ϕ^{ion}	0.3779	87.2566	0.1634	28.4523	0.9206

Table 4.2: Mean residuals, RMS, and Huber weights for the three ionospheric components B_r^{ion} , B_θ^{ion} , and B_ϕ^{ion} for Model A.

In figure 4.2 further details of the fit of Model A to the Swarm data are given in the form of the distributions of the residuals between model prediction of B_r^{ion} , B_θ^{ion} , and B_ϕ^{ion} and Swarm data. The blue dotted lines mark the a-priori assumed data errors σ while the red dotted line represents the mean value of the residuals found in table 4.2. It can be seen that the majority of the residuals are within the assumed error margins indicating the consistency of the assumed errors and results obtained from Model A. The distributions appear to be approximately Laplace distributed due to the long tails and the shape central spike.

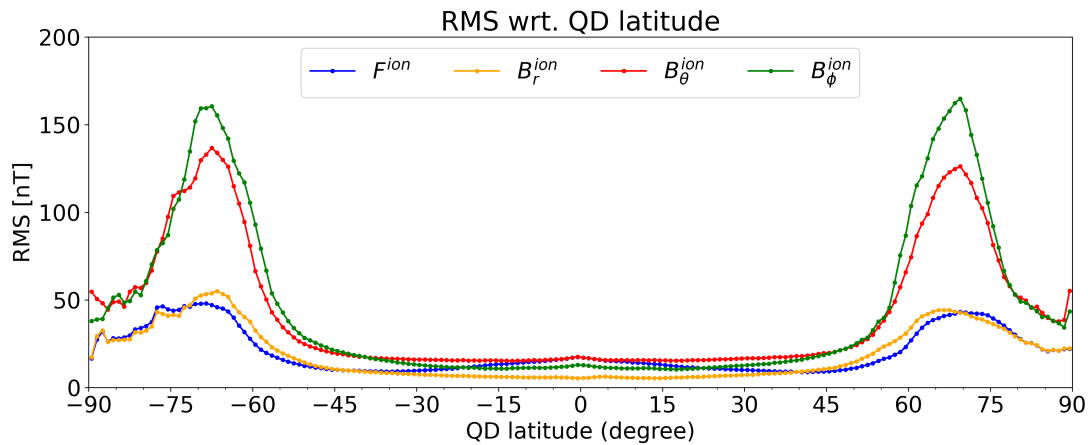


Figure 4.1: RMS values with respect to QD-latitude of the residuals, between model prediction and Swarm data corrected for internal and magnetospheric fields, for the field intensity F^{ion} and the three ionospheric components.

Figure 4.1 summarises the dependence of the RMS residual as a function of the QD-latitude for the field intensity F^{ion} , and the three ionospheric field components. The figure shows that the majority of the residuals are located in the polar region which is also where we have high amplitude and dynamic during substorm activity. The high RMS values in the polar regions implies that the chosen a-priori data error is an underestimate for these two components. However, the RMS for F^{ion} and B_r^{ion} in the polar regions are significantly smaller and seems to stay within 40-50nT indicating the consistency of a-priori data error for B_r^{ion} and F^{ion} .

Figure 4.3 shows further details in polar and global plots of the median residuals plotted in QD/MLT coordinates. It is seen that the majority of large residuals are located around the polar caps. The residuals are largest in the B_ϕ^{ion} component, which coincides with the histograms introduced previously, which is dominated by FAC signatures, and smallest for B_r^{ion} , which is dominated by signatures from horizontal currents.

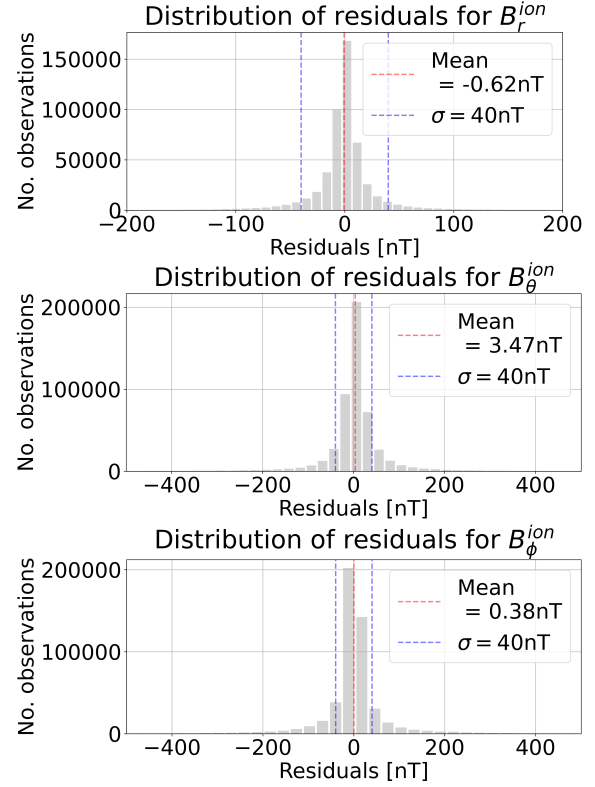


Figure 4.2: Distributions of the residuals between the predictions of Model A and Swarm data for the three field components. The a-priori data error estimates and mean value of the residuals can also be seen in the figures. The few large outliers have been removed in these figures.

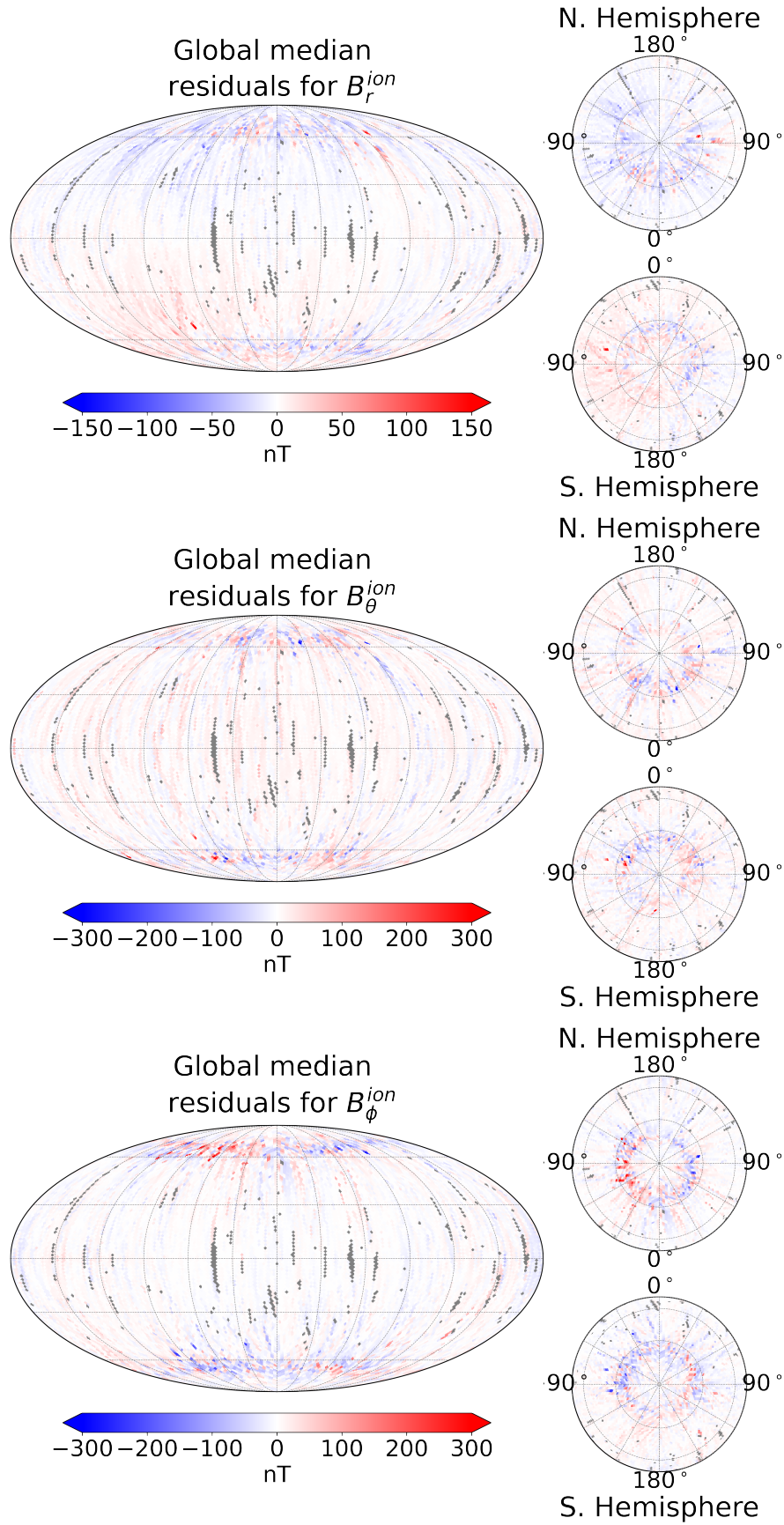


Figure 4.3: Global and polar plots of the median values of the residuals in QD/MLT coordinates. The titles of the plots refer to the variable stored in the datafile. The gray spots are bins with no data.

4.1.3 Typical model properties and ionospheric currents during disturbed conditions

This section presents the properties of Model A under typical conditions, for disturbed times, found in table 3.2. Plots of FAC and DFC under typical conditions will be documented and a summary diagnostics of Model A will be presented.

Table 4.3 contains important summary diagnostics of the model e.g. normalised misfit and average Huber weights values. A $||\delta\mathbf{m}||/||\mathbf{m}|| \sim 0.18\%$ means that the model parameter estimates only change $\sim 0.18\%$ from the 9th to the 10th iteration. This indicates that the model has converged within these 10 iterations.

Model norm FAC (nT) ²	Normalised misfit	$ \delta\mathbf{m} / \mathbf{m} $
$1.2732 \cdot 10^{-6}$	1.0213	$1.7926 \cdot 10^{-3} \sim 0.18\%$

Table 4.3: Model norm, normalised misfit, and the convergence criteria computed for Model A.

Figure 4.4 presents a visualization of the FAC and DFC under typical conditions given in table 3.2. In the plot can be seen the ring-shaped patterns for *R1* and *R2*. The upward part of *R1* can be seen at 68° QD-latitude and 20hr MLT, while the downward *R1* can be found at 68° QD-latitude and 4hr MLT. *R2* appears much weaker and are located at 61° QD-latitude, 10hr MLT for the downward current and at 64° QD-latitude, 4.5hr MLT for the upward current.

In figure 4.5 the horizontal sheet current under typical conditions is presented. The horizontal sheet current is estimated by combining the FAC and the DFC see section 2.3.2 [Laundal, Finlay, Olsen, and Reistad 2018].

Figure 4.6 displays the model predictions of the ionospheric E-layer field components B_r^{ion} , B_θ^{ion} , and B_ϕ^{ion} on global and polar maps for the date 20/01/2015 at 12:00 UTC at a height of 450km. The field predictions at Swarm altitudes are produced by adding the magnetic field produced by the FAC (\mathbf{B}^{tor}) and the magnetic field produced by the DFC (\mathbf{B}^{pol}). From all three figures it can be seen that the ionospheric field is mostly active in the polar regions as expected. A clear two celled pattern is seen in all three figures and there appears to be an asymmetry in the field pattern between the Northern and Southern hemispheres.

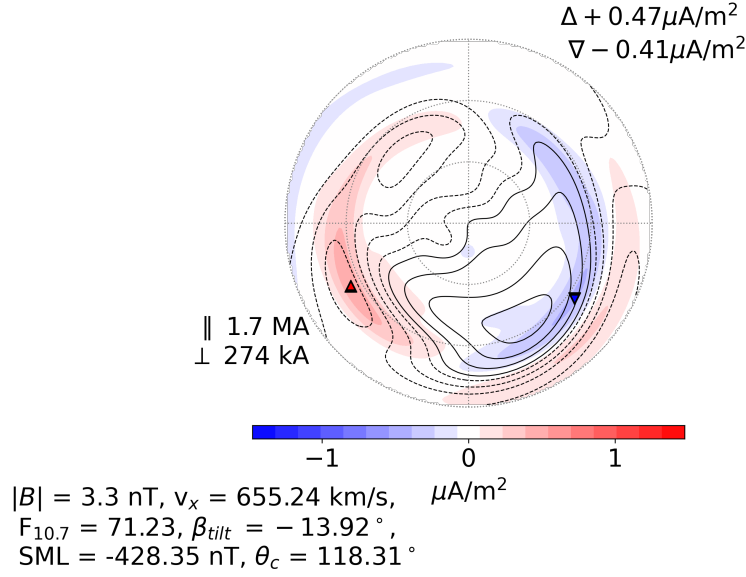


Figure 4.4: Field aligned currents are presented here as red and blue colors and the DFC function is shown as contours for the Northern Hemisphere. The blue color represents the downward current while the red represents the upward current. The dotted contour lines illustrates negative values while the solid lines are positive values of the DFC. The apex north pole is at the center of the plot with QD-latitude circles of 60° , 70° , and 80° marked. The red and blue triangles indicates the placement of the maximum in upward and downward current densities and the value of these can be seen in the top right corner. \parallel represents the scale of the total upward current and \perp is the scale of the total DFC. The input driving conditions are listed in the lower left corner, these are typical of the selected data see table 3.2.

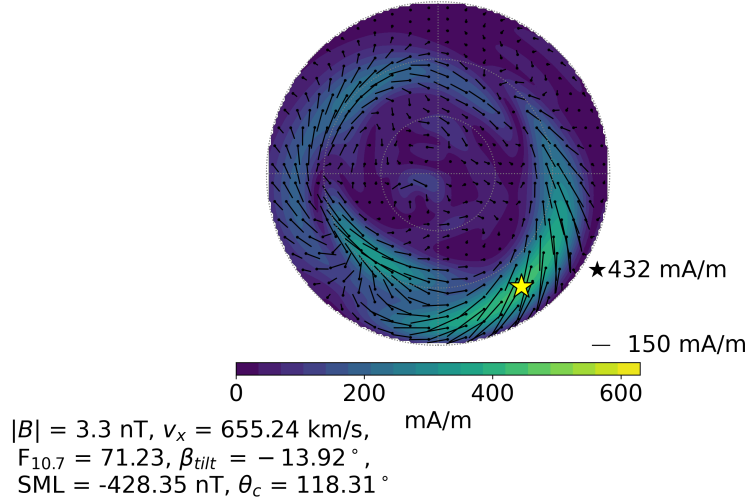
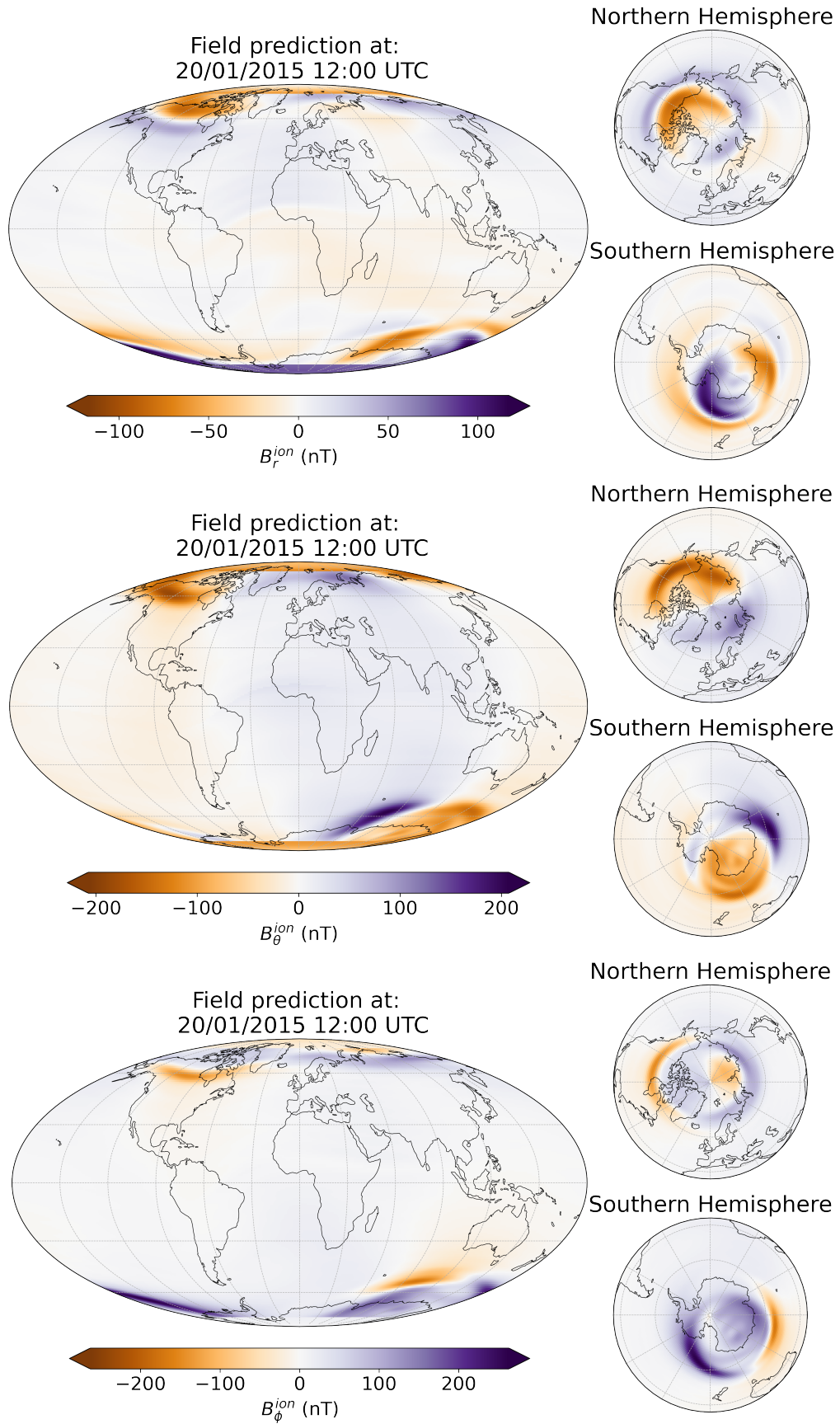


Figure 4.5: A plot of the horizontal sheet currents in the Northern Hemisphere under typical conditions (see table 3.2). The arrows represents the direction and strength of the current, the scale of the arrows can be found in the lower right corner. The colors illustrates the strength of the currents as well. The yellow star represents the peak current. The figure is produced in a similar way as figure 4.4.



4.2 Dynamics during substorms

Having documented the basic structure of the ionospheric currents during disturbed conditions we next move on to describe how the currents change during example substorm events. In particular, we examine the predictions of Model A during two substorms, comparing these with the Swarm data collected during these events.

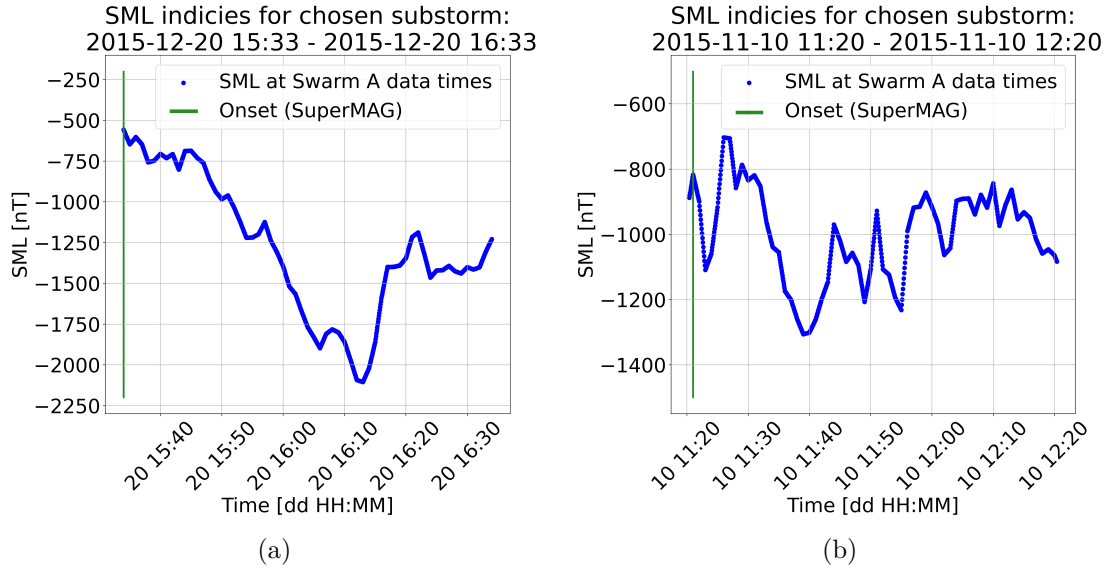


Figure 4.7: Plots of the interpolated SML index for a large substorm (a) and for a standard size substorm (b). The green line represents the onset time for each substorm.

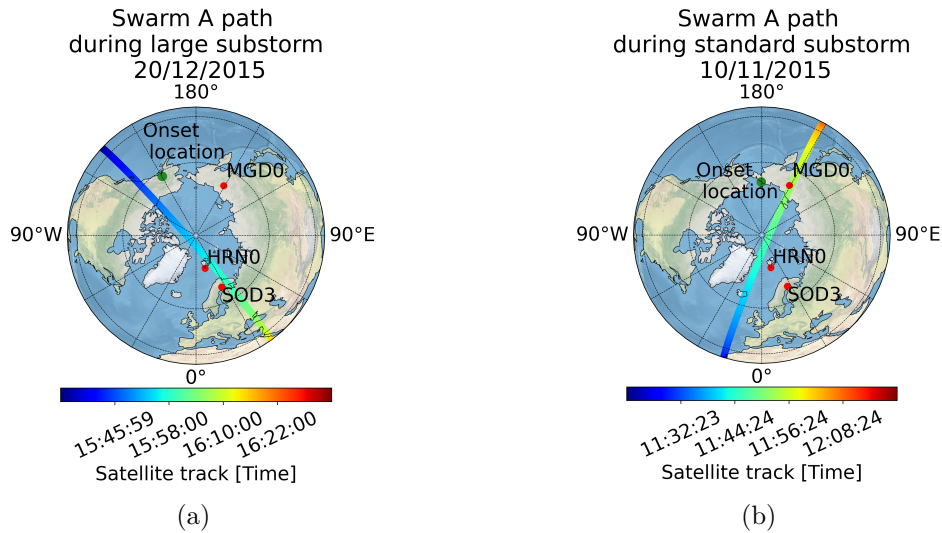


Figure 4.8: Polar plots of the satellite Swarm A's track during the large substorm at 20/12/2015 (a) and standard substorm at 10/11/2015 (b). The satellite's path is marked with a colorbar illustrating the time at each location. The green dot represents where the onset, for each of the two substorms, was measured by a ground observatory. The red dots represent the location of three ground observatories Hornsund (HRN) in Norway, Sodankyla (SOD) in Finland, and Magadan (MGD) in Russia.

Using the substorm list from Newell and Gjerloev two example substorms have been chosen. The onset times are compared to the satellite location in figure 4.8. Substorms can last for several hours but in this section only the time interval that the satellite is in the polar cap/auroral oval is displayed and used. Hence the term "beginning" and "end" of a substorm corresponds to the entrance and exit of the polar cap/auroral oval for the satellite.

The first event is from 20/12/2015 with an onset time of 15:40 UTC and is a relatively *large* substorm with *SML* values below -2000nT. A plot of the interpolated *SML* index with respect to time can be seen in figure 4.7a. The second event is from 10/11/2015 with an onset time of 11:33 UTC. This substorm will be referred to as the *standard* substorm since the amplitude of the *SML* index (around 500nT) is the typical amplitude of substorms found in the dataset. The interpolated *SML* index for this substorm can be seen in figure 4.7b.

Figure 4.9 and 4.10 display the model predictions for the magnetic field caused by the FAC \mathbf{B}^{FAC} , the DFC \mathbf{B}^{DFC} , and the total ionospheric prediction $\mathbf{B}^{ion} = \mathbf{B}^{FAC} + \mathbf{B}^{DFC}$ where data is recorded by Swarm A during the time of the substorm. The blue line represents Swarm A data used as input to the modelling, found by subtracting estimates of the magnetic field caused by the magnetosphere \mathbf{B}^{mag} and the internal sources \mathbf{B}^{INT} from the measured magnetic field \mathbf{B}^{data} .

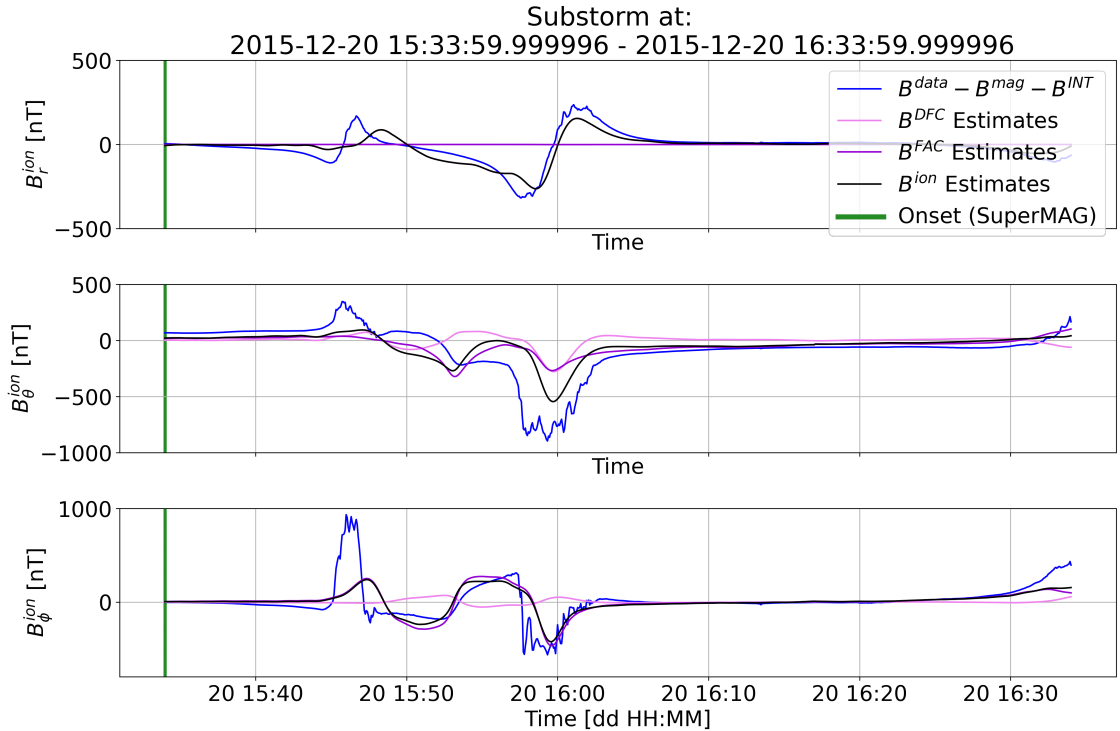


Figure 4.9: Timeseries for magnetic field predictions \mathbf{B}^{DFC} , \mathbf{B}^{FAC} , and \mathbf{B}^{ion} compared to the measured field \mathbf{B}^{data} , where estimates of the internal and magnetospheric sources are subtracted, for the large substorm.

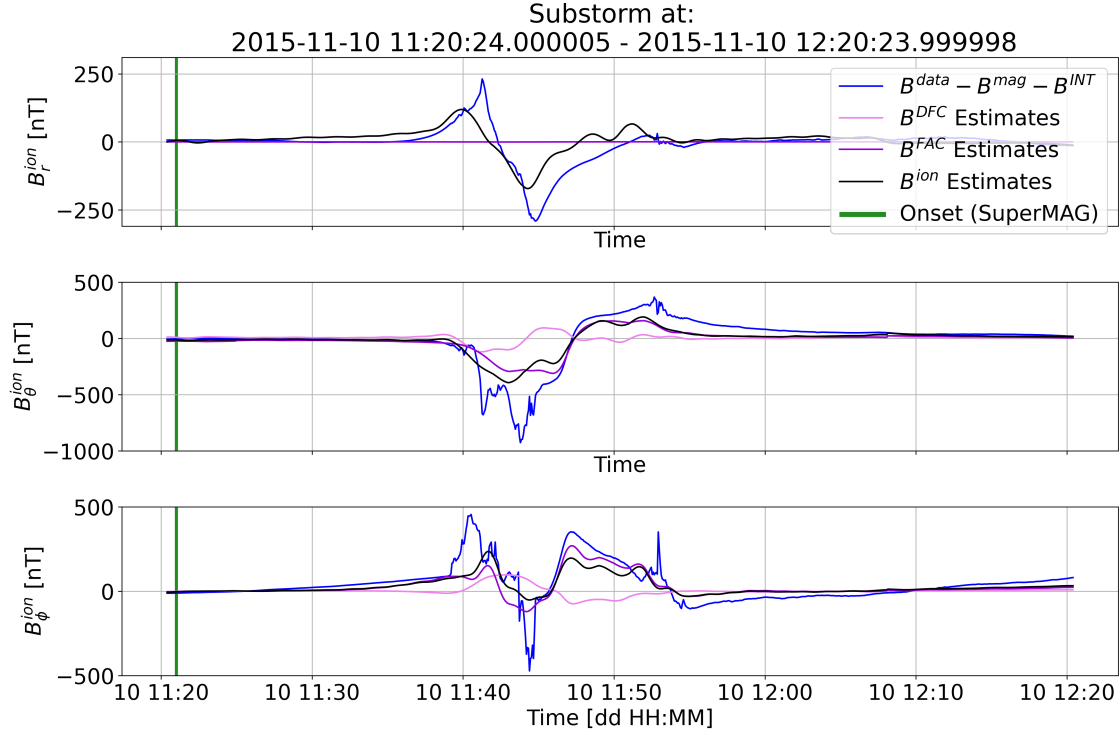


Figure 4.10: Timeseries for magnetic field predictions, made by Model A, \mathbf{B}^{DFC} , \mathbf{B}^{FAC} , and \mathbf{B}^{ion} compared to the measured field B^{data} , where estimates of the internal and magnetospheric sources are subtracted, for the standard substorm.

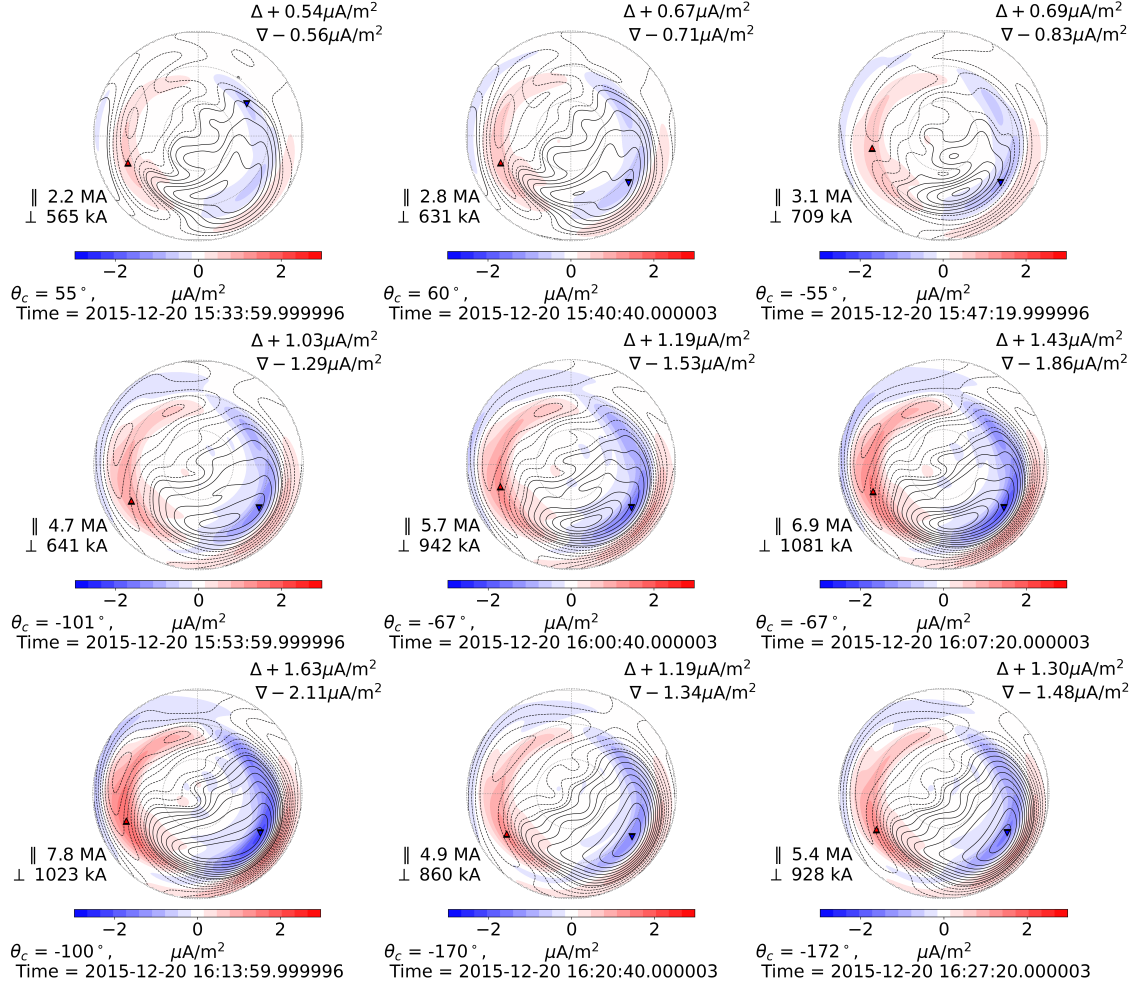


Figure 4.11: Plot of the FAC and DFC during a large substorm at 20/12/2015 made by Model A, where the external parameters vary with time. The clock angle and timestamp are shown in the bottom left corner of each plot.

For the large substorm the dynamics of the global patterns of FAC and DFC plotted with respect to clock angle in figure 4.11 as a time sequence during the substorm. There is a gradual amplification in both the FAC and DFC until 16:13 UTC where the maximum amplitude is reached, afterwards the strength dims down again. The structure of the currents also change during the substorm; at first the DFC pattern is rather complex but becomes more structured as the amplitude of the currents increase. The positive values of DFC starts to align with the downward FAC around R1 while the negative values of the DFC starts aligning with the upward FAC in R1, as the time elapses.

Figure 4.12 shows a similar time sequence of the horizontal sheet current plotted for the large substorm at the same times as for figure 4.11. At the beginning of the substorm the sheet current has a high amplitude but as the time progresses the amplitude decreases. At 16:13 UTC the current amplitude has reached its minimum. At and after 16:13 UTC the maximum amplitude, of the horizontal current, has moved down from 70° magnetic latitude to 60° magnetic latitude.

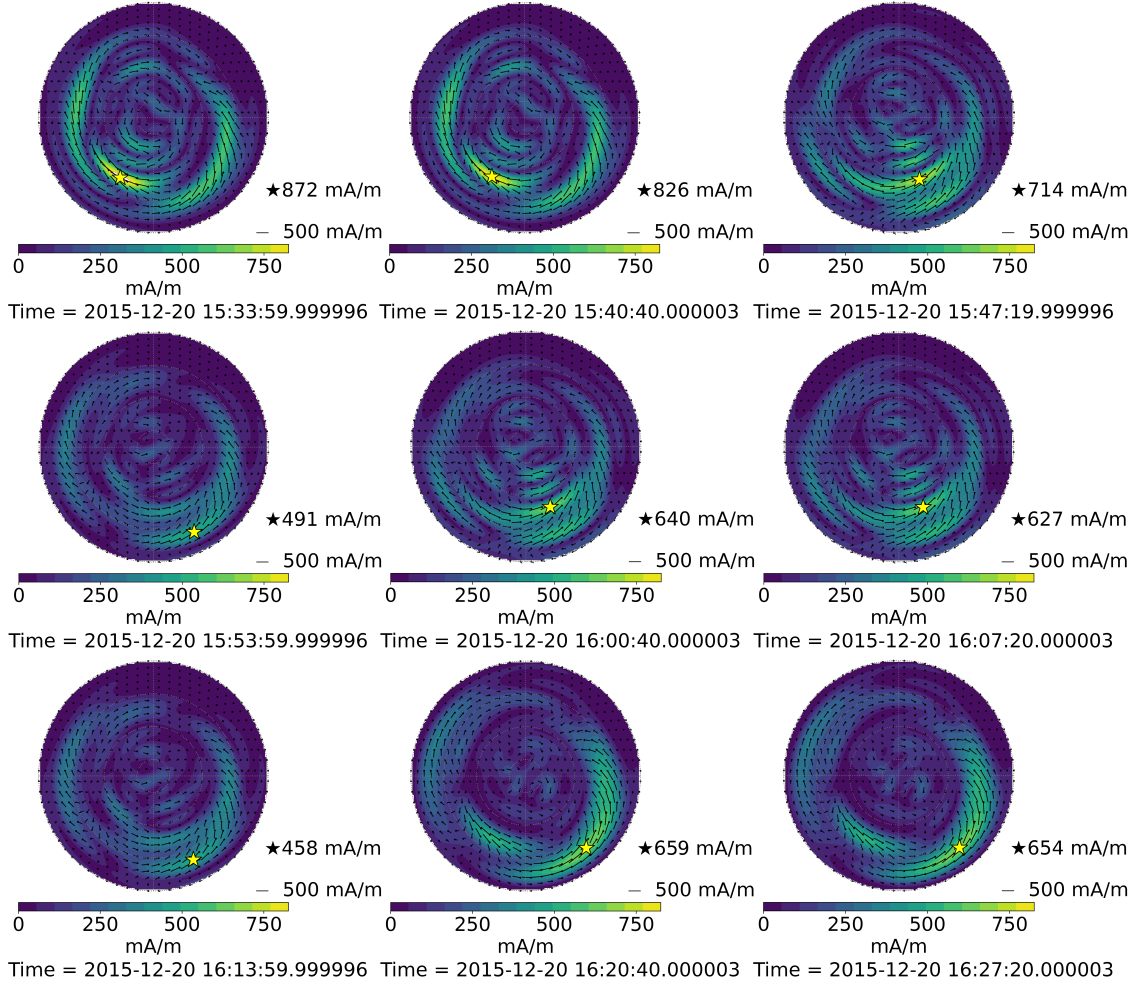


Figure 4.12: Plots of the horizontal sheet currents during the large substorm event at 20/12/2015 made by Model A, where the external parameters vary with time. The timestamps are shown in the bottom left corner of each plot and the minimum latitude is here set to 55° .

4.3 Comparison with independent observations during an example substorm event

In the previous section the predictions of Model A were compared to dependant data from Swarm A. In this section the model performance is examined by comparing it to independent data. Section 4.3.1 documents a comparison between Model A predictions to independent satellite data from Swarm A. Independent ground observatory data from three stations will be compared to the model predictions in section 4.3.2.

4.3.1 Comparison to independent satellite data

Figure 4.14 shows the model predictions B^{ion} , made by Model A, and Swarm A data from the period 24/12/2020 at 15:00 UTC to 16:40 UTC during a substorm at 15:11 UTC. The Swarm data is outside the scope of the data used for the field modelling of Model A making the Swarm data independent.

In figure 4.13 is shown the satellite's path during the substorm at 24/12/2020. The satellite flies straight across the North pole and hence through the auroral oval and polar cap.

The ionospheric model prediction in figure 4.14 is roughly following the measured data in all three components. The model, however, seems to struggle reaching the same amplitudes values as the measured signals. This will be further discussed in chapter 5.

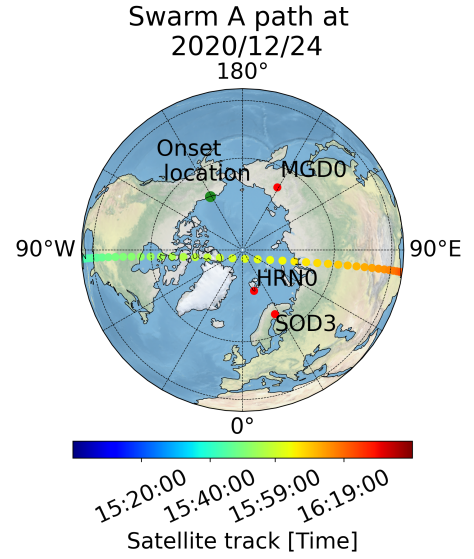


Figure 4.13: Polar plot of Swarm A's path at 24/12/2020 that is illustrated with a colorbar-track representing the time at each location.

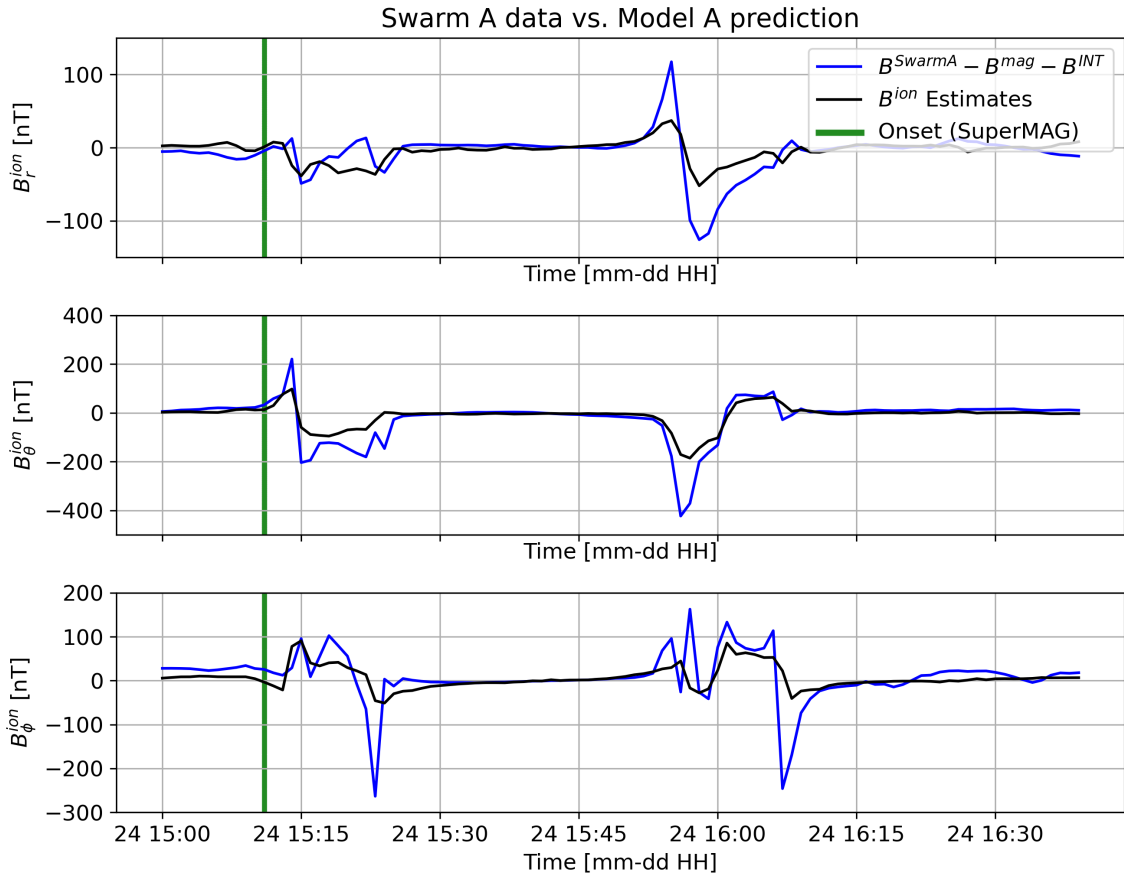


Figure 4.14: Timeseries of model predictions (Model A) and independent Swarm A data for the magnetic field components at a height of 400km. The time interval is from a period outside the dataset used for the construction of the model.

4.3.2 Ground observatory comparison

In figure 4.8 three ground observatories, relatively close to the Swarm A path, are marked. Hornsund (HRN) in Norway is located at 77° latitude and 15.55° longitude. Due to the high northern location, HRN might not be in the auroral oval during the two substorms. Hence a station in Sodankyla (SOD) in Finland located at latitude 67.37° and longitude 26.63° and a station in Magadan (MGD) in Russia at latitude 59.97° and longitude 150.85° are chosen as well.

At ground only the ionospheric field produced by the DFC can be seen and thus \mathbf{B}^{DFC} is the total model prediction for the ground stations. Figure 4.15 and 4.16 show timeseries of the modelled ionospheric field \mathbf{B}^{DFC} during the day 20/12/2015 where the green vertical line represents the onset for the large substorm. The internal field \mathbf{B}^{INT} and the field caused by the magnetosphere \mathbf{B}^{mag} have been subtracted from the observatory data \mathbf{B}^{HRN} and \mathbf{B}^{SOD} , for HRN and SOD respectively. The model predictions deviates from the observatory data at both HRN and SOD. In particular the models struggles at fitting the high amplitude peaks. This will be further discussed in chapter 5.

Figure 4.17 and 4.18 presents the ionospheric field predictions alongside with the measurements taken from HRN and MGD at 10/11/2015. For HRN the model cannot fit the high peaks at 15:00 - 18:00 UTC. For MGD the B_r^{DFC} does a better job at fitting the data but fails in fitting the B_θ^{ion} and B_ϕ^{ion} . This will be further discussed in chapter 5.

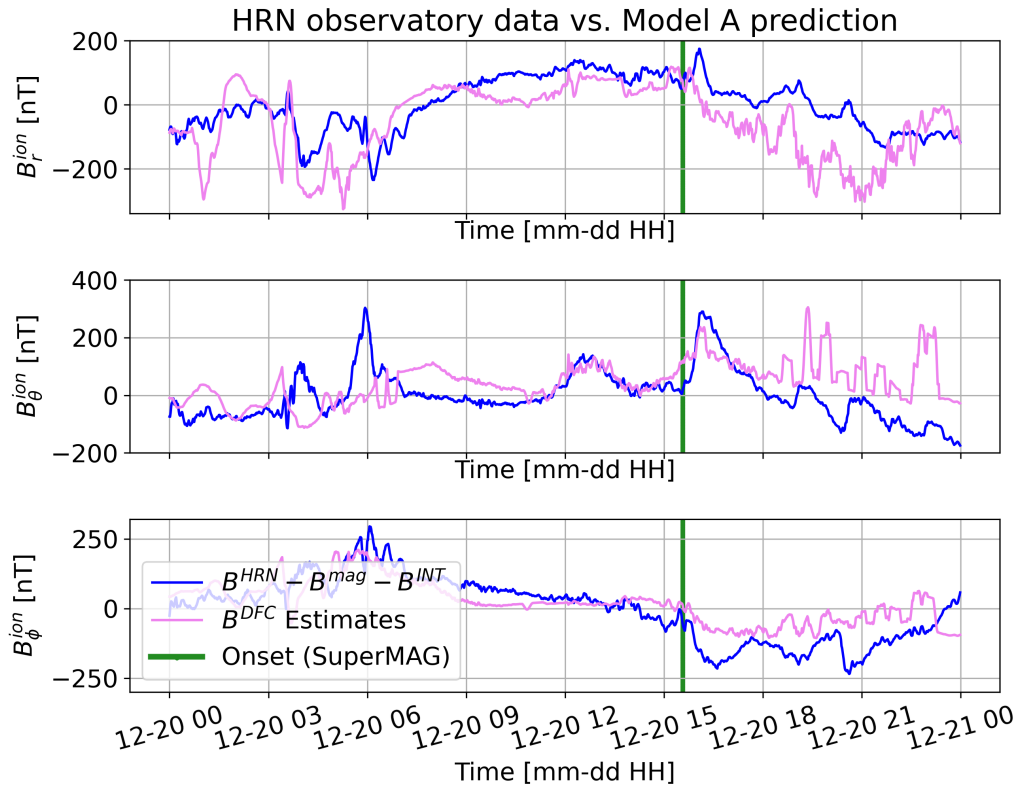


Figure 4.15: Magnetic field measurements from HRN in Norway taken at 20/12/2015 compared to Model A predictions of the ionospheric field seen at ground. The green line represents the time of the onset for the large substorm.

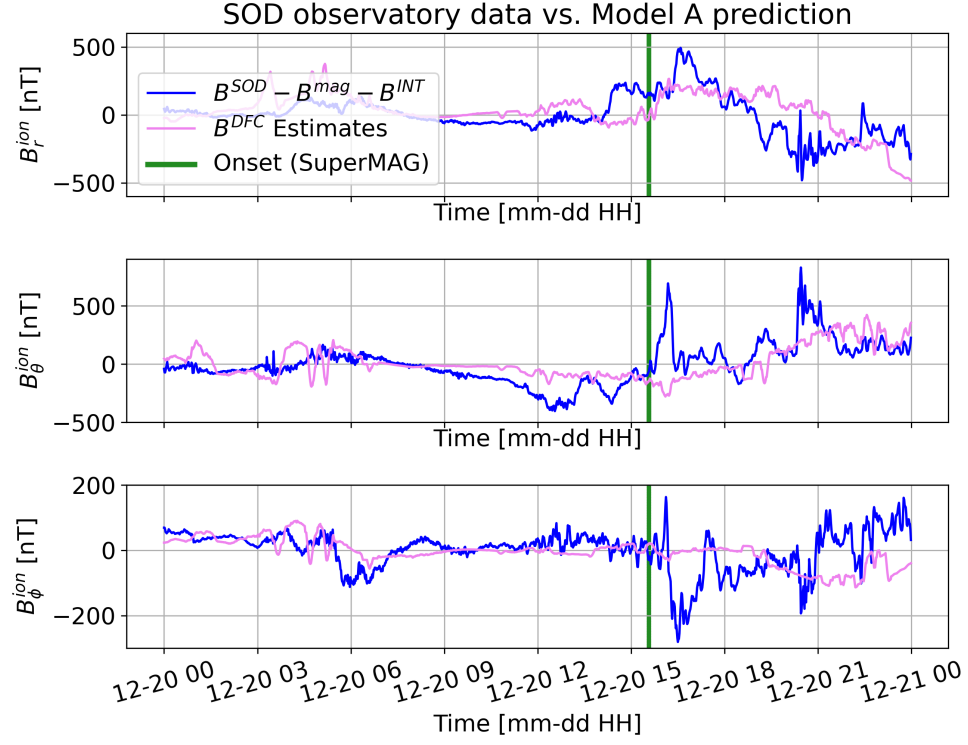


Figure 4.16: Magnetic field measurements from SOD in Finland taken at 20/12/2015 compared to Model A predictions of the ionospheric field seen at ground. The green line represents the time of the onset for the large substorm.

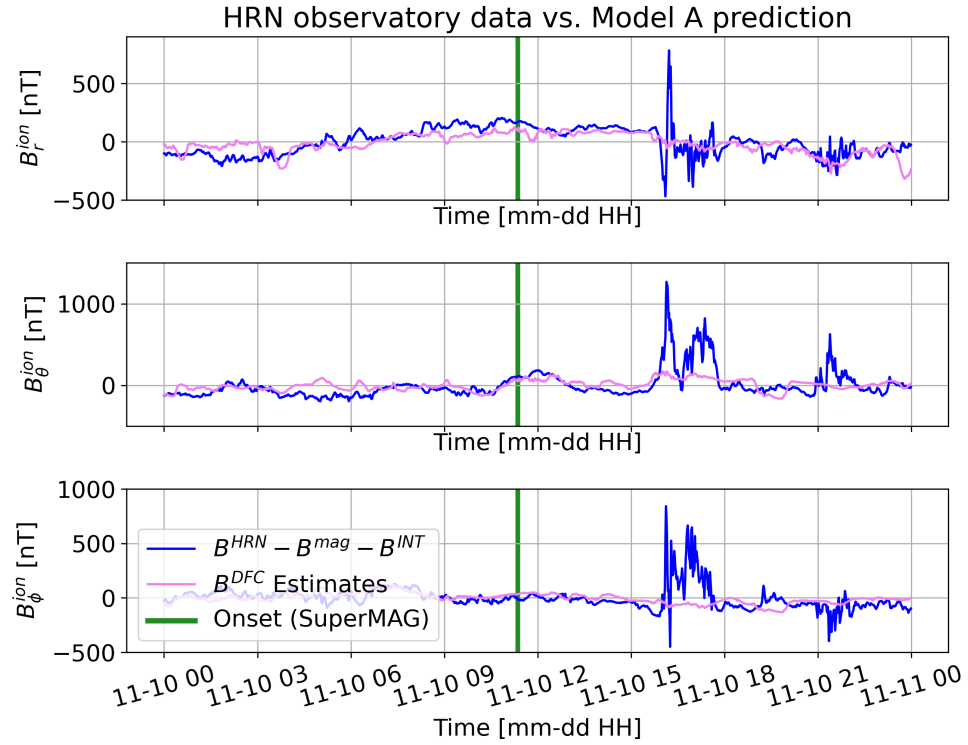


Figure 4.17: Magnetic field measurements from HRN in Norway taken at 10/11/2015 compared to Model A predictions of the ionospheric field seen at ground. The green line represents the time of the onset for the large substorm.

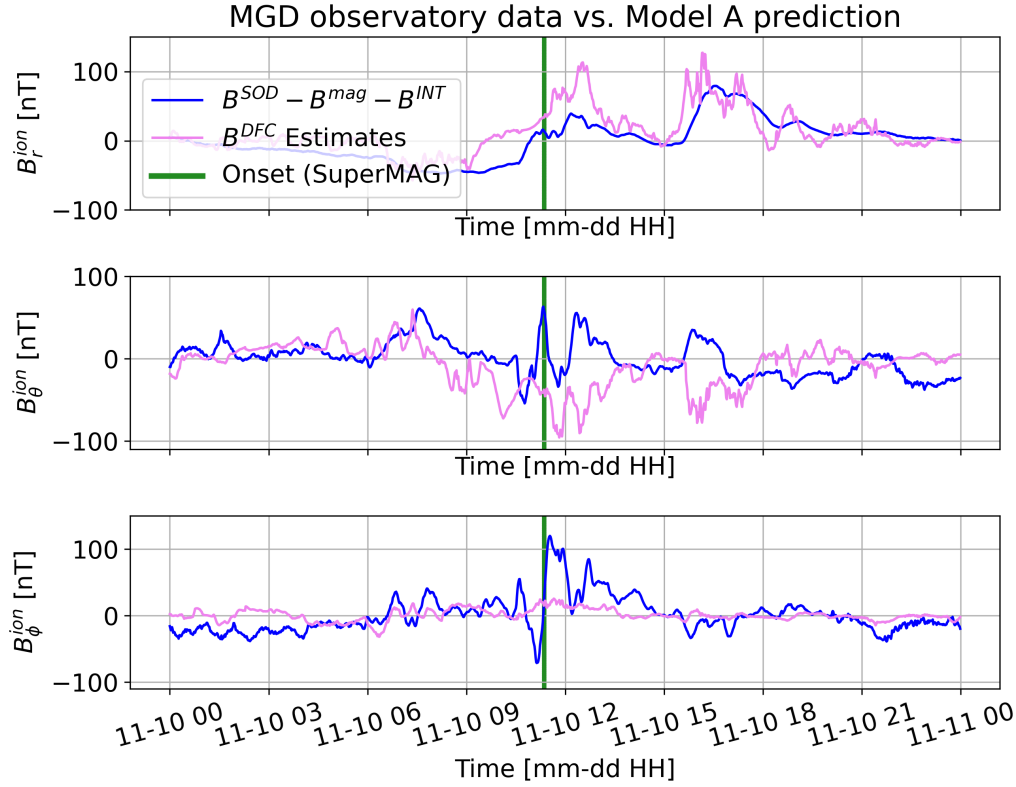


Figure 4.18: Magnetic field measurements from Magadan (MGD) in Russia taken at 10/11/2015 compared to Model A predictions of the ionospheric field seen at ground. The green line represents the time of the onset for the standard substorm.

4.4 Testing alternative datasets

In this section an alternative dataset will be tested. The alternative dataset is derived using Swarm A data in the same time period as before (2014-2017) but a different data selection criteria is chosen. To see this selection criteria see Appendix A.6. In principle the selection criteria uses the same onset determination as Model A but here it sets a threshold for the *SML* index. The threshold is used to determine when to stop including data i.e. when the substorm has ended. For this model the selection criteria stops when 50% of the onset *SML* value is restored or when 3 hours have passed. With this approach 17% of the original data is kept and stored in the datafile. This model will be referred to as Model B.

Variable	Mode of distribution
SML	-267.00 nT
v_x	420.18 km/s
B_{IMF}	3.28 nT
$B_{IMF,y}$	2.23 nT
$B_{IMF,z}$	-2.09 nT
F10.7	72.12 sfu
Tilt angle β_{tilt}	-13.91°
Clock angle θ_c	117.97°

Table 4.4: Mode of distributions for Model B.

For Model B the mode of the distributions can be found in table 4.4. The mean of the residuals, the RMS, and the Huber weights can be found in table 4.5. The convergence, normalised misfit, and model norm for Model B is shown in table 4.6. The RMS values for the three magnetic field components and the intensity F^{ion} for the ionospheric field is shown in figure 4.19.

Model B	Mean of residuals (nT)	RMS (nT)	Mean of weighted residuals (nT)	Weighted RMS (nT)	Mean of Huber weights
B_r^{ion}	-0.2051	22.0294	0.1674	10.9066	0.9919
B_θ^{ion}	2.2068	55.0815	1.9184	20.5232	0.9555
B_ϕ^{ion}	-0.0825	66.6818	-0.1292	22.6905	0.9440

Table 4.5: Mean of residuals, RMS, and Huber weights for the three ionospheric components for Model B.

Model norm FAC (nT) ⁻²	Normalised misfit	$ \delta\mathbf{m} / \mathbf{m} $
$5.8749 \cdot 10^{-6}$	0.6246	$1.1163 \cdot 10^{-4} \sim 0.01\%$

Table 4.6: Model norm, normalised misfit, and the convergence criteria for Model B.

The large substorm presented in the previous sections are shown in figure 4.20 with field predictions for Model A and Model B alongside with satellite data from Swarm A. The difference in Model A and Model B predictions are quite small and Model B does not seem to fit the Swarm data significantly better than Model A despite the lower misfit and RMS. This will be further discussed in chapter 5.

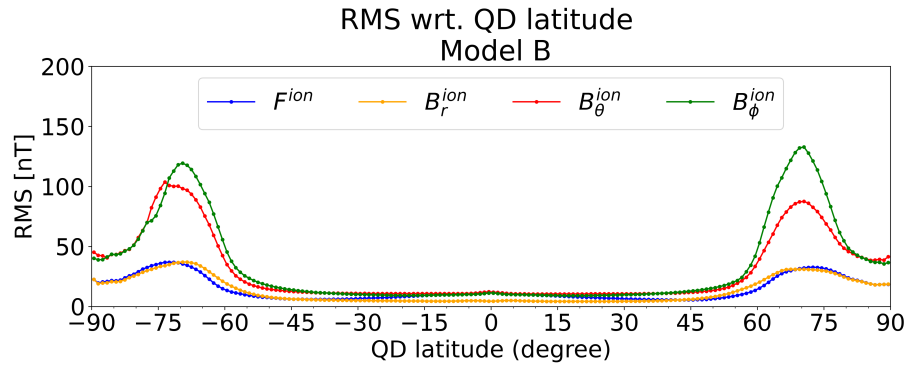


Figure 4.19: RMS values for residuals between model prediction and Swarm data with respect to QD-latitude for the field intensity F^{ion} and the three ionospheric components for Model B.

The magnetic field measured at the ground observatories HRN and SOD, during the large substorm, is also compared to the model predictions for Model A and Model B in figure 4.21 and 4.22. Similarly as for the Swarm data Model B does not seem to perform a significantly better job than Model A in fact they seem to perform equally bad for both stations.

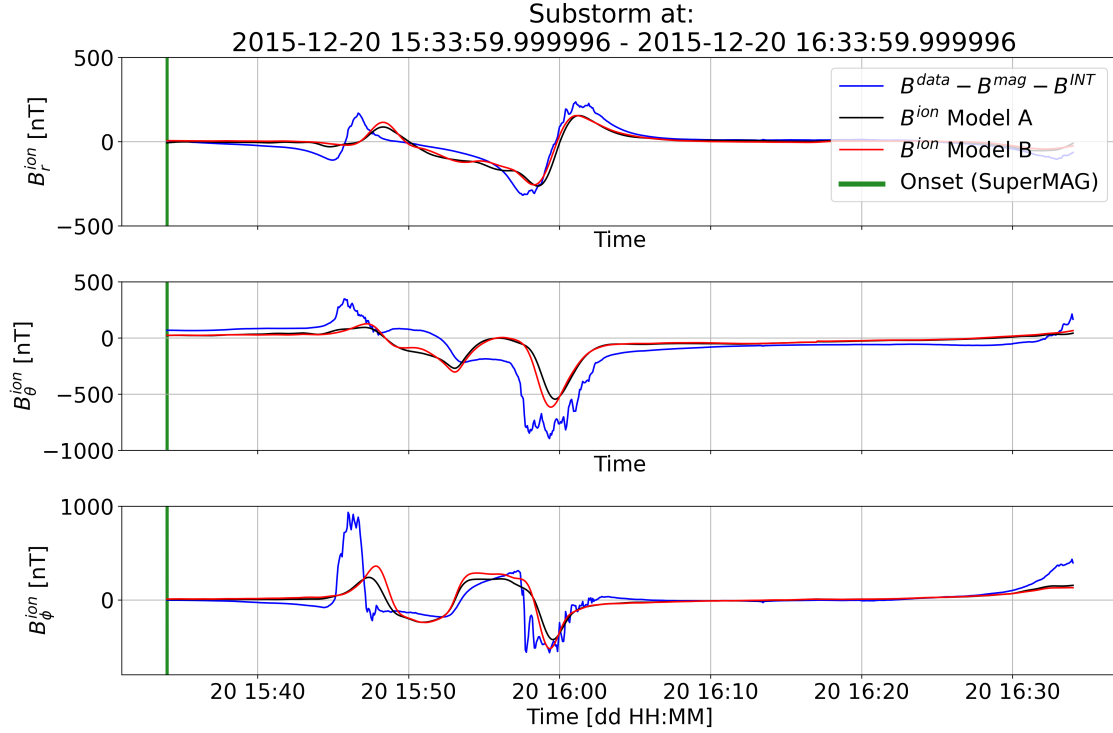


Figure 4.20: Timeseries for magnetic field predictions, made by Model B, \mathbf{B}^{DFC} , \mathbf{B}^{FAC} , and \mathbf{B}^{ion} compared to the measured field B^{data} , where estimates of the internal and magnetospheric sources are subtracted, for the large substorm.

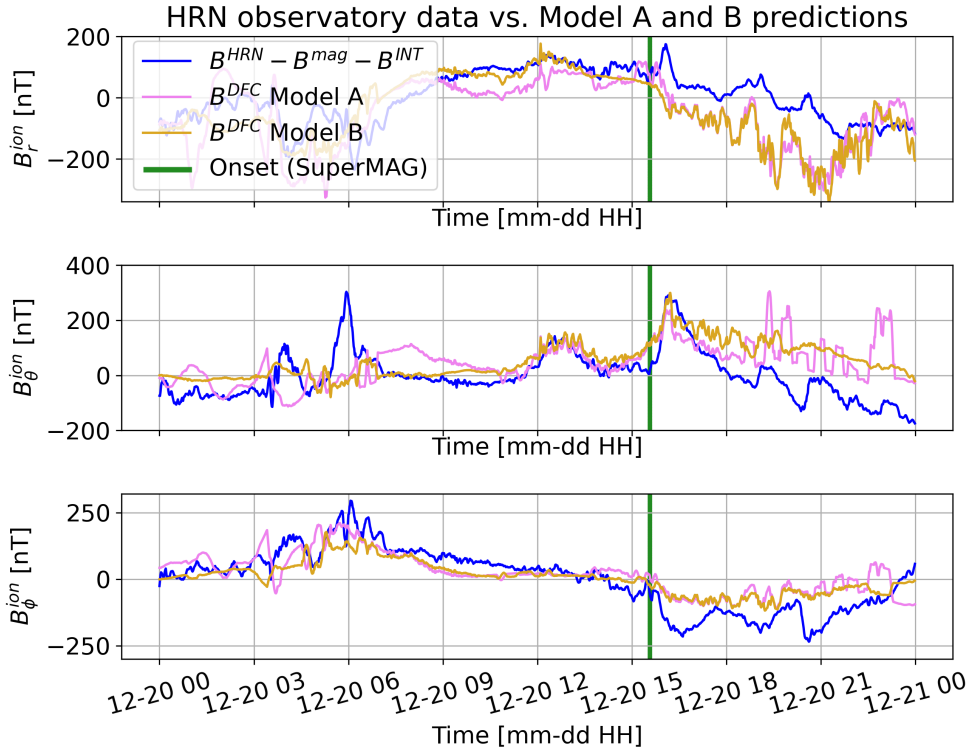


Figure 4.21: Magnetic field measurements from HRN in Norway taken at 20/12/2015 compared to Model A and Model B predictions of the ionospheric field seen at ground. The green line represents the time of the onset for the large substorm.

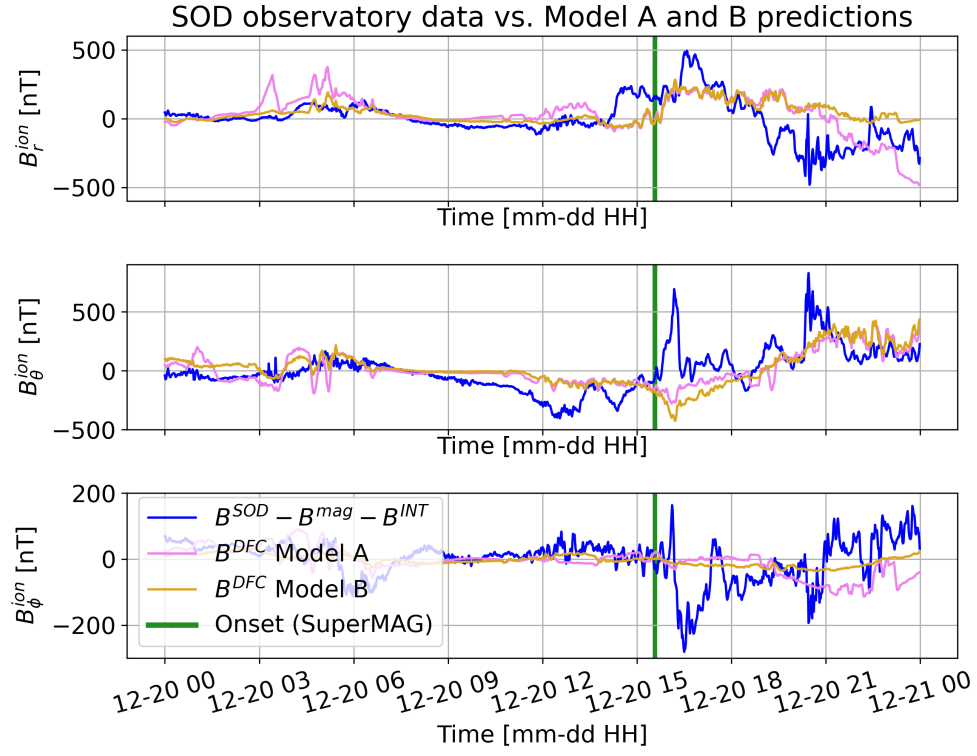


Figure 4.22: Magnetic field measurements from SOD in Finland taken at 20/12/2015 compared to Model A and Model B predictions of the ionospheric field seen at ground. The green line represents the time of the onset for the large substorm.

Discussion

This chapter will evaluate and discuss the results presented in the previous chapter. Section 5.1 will evaluate the fit of Model A to the contributing Swarm data, including a discussion of residuals. Section 5.2 discusses the model performance during typical conditions while section 5.3 evaluates the model performance during substorm activity. An assessment of the agreement of the model predictions and independent data is carried out in section 5.4. The influence of the *SML* index on the ionospheric field model is investigated in section 5.5 and finally recommendations and suggestions for future work are presented in section 5.6.

5.1 Fit of Model A to Swarm data

In section 4.1.2 it was shown that the model fits Swarm A data better in the B_r^{ion} component than in the B_θ^{ion} and B_ϕ^{ion} components. This was seen in table 4.2, in figure 4.2, and in figure 4.1 where we found smaller residuals and a smaller RMS value for the B_r^{ion} component. This is expected because B_θ^{ion} and B_ϕ^{ion} are affected by FACs which have less effect on B_r^{ion} . The FACs are known to be very dynamic and can be of small scale and hence they are not easily captured by the large-scale model, constructed here, which is an average of the ionospheric field for a given set of driving parameters.

It is also seen in figure 4.3, that shows what part of the data that is not explained by the model, that large residuals, in polar regions, are significantly high for B_θ^{ion} and B_ϕ^{ion} . The polar regions, and in particular the auroral oval, are places where there are intense, small-scale and highly dynamic currents [Kepko et al. 2015] and hence higher errors in these regions are expected. This implies that the model cannot fully explain the processes in this part of the ionospheric magnetic field.

Furthermore, table 4.3 showed a change-rate of $\sim 0.18\%$ for Model A and it was concluded that the model had converged. If the model has not completely converged it will affect the model accuracy. It could be argued that the model needs a few more iterations to bring down the change-rate even further in order to make sure that the model has fully converged. However the drawback here is that it will increase the model computation time.

5.2 Evaluation of model performance under typical conditions

For typical conditions Model A seems to perform according to the presented theory by Milan et al. 2017. A distinct ring pattern, for the FACs, appears where the inner ring ($R1$) is the strongest and the outer ring ($R2$) the weakest (seen on figure 4.4) which is what we would expect to see according to Milan et al. 2017. Furthermore, the DFC also seems to have a distinct pattern that seems to be correlated with the FAC maximums.

The horizontal sheet current, modelled by Model A under typical conditions, is also in agreement with the expected outcome (Milan et al. 2017). The convection electrojets, seen in figure 4.5, consist of an eastward and westward electrojet with a maximum amplitude of 432 mA/m. These electrojets are mainly consisting of the Hall currents that are generated by the downward FAC.

Investigating the total ionospheric field prediction of Model A, under typical conditions in figure 4.6, we find that all three components show a two celled pattern in field strength. Often, in the published literature, only the Northern polar region is shown however figure 4.6 clearly shows a difference in the pattern and strength between the Northern and Southern hemispheres indicating polar asymmetry in the ionospheric field for all three components. This is likely due to the differences in solar illumination, and hence ionospheric conductivity in the two hemispheres. The global maps also show that the ionospheric field is mainly active at the auroral oval at the polar regions.

5.3 Evaluation of model performance during substorms

The performance of Model A was tested during two substorm events: one large substorm at 20/12/2015 15:40 UTC and one of standard size substorm at 10/11/2015 11:33 UTC. For the large substorm, seen in figure 4.9, Model A has a seemingly good fit of B_r^{ion} . As mentioned B_r^{ion} is dominated by signatures from the DFC and hence the DFC part appears to be well resolved in by the model. The peak at the beginning of the substorm (around 15:45) is poorly resolved in all three components. One reason for this could be that such peaks do not always appear in substorms for these solar wind driving and SML input parameters, at least for the dataset used for the development of Model A. Hence the model may not be able to predict this event very accurately. It is expected that the model has a less accurate performance for large substorms since the primary substorm data, used for the modelling, consists of smaller events.

During the standard substorm, seen in figure 4.10, the predictions of Model A seem, overall, to fit the data relatively well. The sharp peaks in the substorm are, however, again poorly resolved by the model. This suggests that the model still lacks important factors for substorm dynamics or has insufficient spatial resolution to capture small scale feature seen in the observations.

Investigating figure 4.11 we see that an increase in amplitude for the FAC happens in both $R1$ and $R2$ during the large substorm which is a behavior that we expect to see during substorms. The highest value of the FAC is found at 16:13 UTC which approximately corresponds to the minimum SML value as seen in figure 4.7a. The DFC goes from having a complex pattern to align with the FAC and gain a more structured pattern.

Figure 4.12 shows the horizontal sheet current during the large substorm. A clear change in pattern and amplitude is seen as time advances. The yellow star marks the place of maximum current density which seems to move down towards lower latitudes during the course of the substorm. A dimming of the horizontal currents is also seen at 16:13 which is where the FAC is at its maximum amplitude.

5.4 Fit of Model A to independent data

A way of testing the performance of the model is by making comparisons to independent data e.g. ground observatories and Swarm data taken outside the scope of the dataset, used to produce Model A. During a substorm event at 24/12/2020 measured by Swarm A a model prediction was made, the result can be seen in figure 4.14. The model is roughly following the same trend as the data measured from Swarm. However the model seems to struggle reaching the same peak amplitudes as the measurements. An improvement of the model could be made by including data from more years and in that way training it to model substorm dynamics based on a broader range of events.

Comparisons to ground observatories, seen in figures 4.15, 4.16, 4.17, and 4.18, show that Model A deviates from the measured station data. Model A is clearly not able to model the signals for B_{θ}^{ion} and B_{ϕ}^{ion} appearing right after the substorm onset. This strongly indicates limitation of the model. One explanation for the large deviations in amplitude of the signals is that the model does not consider the induced currents in the Earth's mantle. Far away from the Earth's surface, e.g. at Swarm altitude, the signals coming from the induced currents in the mantle are very weak. Ground observatories are stationary and are placed at the surface of the Earth and hence are more likely to pick up these signals. Thus the magnetic field contribution from the induced currents appear in the station data but not in the model itself. The absence of signals, also seen in the observatory comparison, is likely due to unresolved small scale behaviour or non-typical dynamical features in any given substorm.

5.5 Controlling factors in the model

A factor that separates this modelling procedure from previously published models e.g. the AMPS model (Laundal, Finlay, and Olsen 2016) is the inclusion of the extra external parameter SML . By varying the SML index while fixing all other external parameters we can investigate the influence of this parameter.

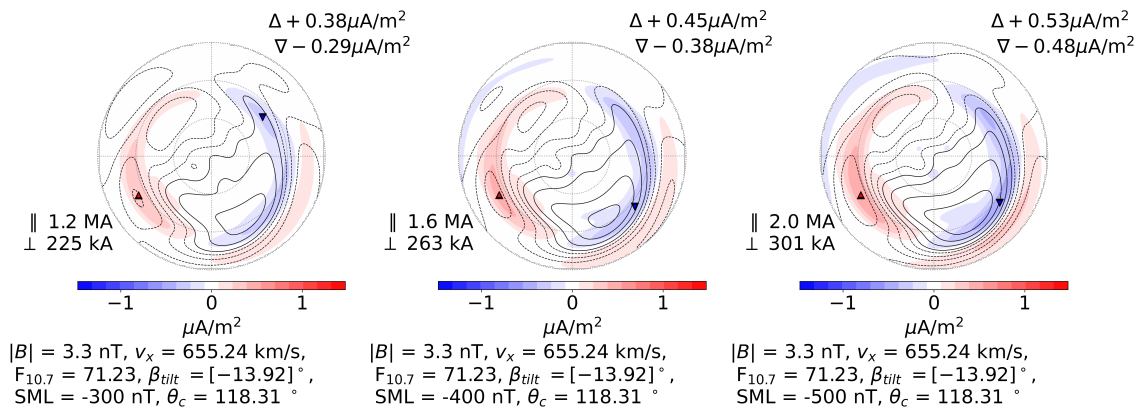


Figure 5.1: The impact of varying the SML index -300 nT (a), -400 nT (b), and -500 nT (c) for FAC and DFC. The rest of the external parameters are fixed and set to the typical values as seen in table 3.2.

The *SML* index were introduced in the model as a measure of the auroral electrojet activity. The convection auroral electrojets are connected to the FAC and thus making the *SML* index an important factor. The importance is illustrated in figure 5.1 here it is shown how both the amplitude of the FAC and the pattern of the DFC is effected by the changing *SML*. It indicates that *SML* is indeed a crucial factor in controlling the ionospheric field models we have developed of the ionospheric dynamic.

5.6 The influence of data selection

Model B is a model created with an alternative dataset explained in appendix A.6. The dataset is from the same timespand 2014-2017 but includes data from all detected onsets. This results in a dataset with 5,413,183 datapoints for Model B in contrast to the 501,289 datapoints used in the development of Model A.

The RMS values for Model B seen in table 4.5 are noticeable smaller than those of for Model A both in the weighted and un-weighted case. The Huber weights are also slightly higher which means more data is given a higher weight. In the plot of the RMS with respect to QD-latitude, figure 4.19, we see that the RMS is still highest at polar latitudes but are smaller than the results for Model A. This indicates that Model B has a general better fit to the selected data than Model A. However it should be noted that Model B might contain far more quiet-time data than Model A which will influence the estimates.

In table 4.6 a convergence of $\sim 0.01\%$ is reached after 10 iterations in contrast to the $\sim 0.18\%$ of Model A. In general it is desired that the change-rate of the model parameters is, with iteration number, as small as possible. A way of testing this is by investigating the predictions made by Model B.

Figure 4.20 shows the model predictions of Model A and B compared to the measured Swarm data. It appears that Model B does not perform significantly better than Model A regarding predictions during the substorms. Similarly this is also not the case for the prediction of the ground observatory data in figure 4.21 and 4.22.

The normalised misfit, convergence, and RMS values have improved from Model A to Model B however the model performance for data and substorm predictions is not significantly different. This means that changing the selection scheme has not supplied the model with improved knowledge about the dynamics of a substorm; this seems to be limited by the current model parameterisation.

5.7 Recommendations and Future work

In the above sections the successes and limitations of the model have been discussed. Even though the model provides promising results there are still obvious improvements needed to obtain better models of the typical behaviour of the ionospheric field during disturbed conditions. In this section a few recommendations for future work will briefly be outlined.

Model A is constructed by a data selection scheme that removes a substantial amount of datapoints. Due to the small time interval of the dataset (2014-2017), this induces a somewhat imperfect global coverage and limited constraints regarding some ranges of input parameters that may be visited, especially during large substorms. This limits the

performance of the model predictions. It was tested, with Model B, that including data from more onsets, and hence data from smaller substorms from the same time period, did not improve the model predictions during substorms. Instead for the future it is recommended to include data from more years and most importantly data from several different satellites such as Swarm B, C, and CHAMP. Especially CHAMP data might be useful since it was collected at lower altitude, closer to the E-layer currents, than Swarm data.

Figure 4.2 shows that all three histograms have long tails which is a feature of Huber and Laplace distributions. The model assumes a Huber-distribution of errors but the sharp central spike of all three histograms indicates a Laplacian error distribution may be more appropriate. In future work it might therefore be worth considering a Laplacian weighting-scheme instead of the Huber weighting.

It was noted that the a-priori error, $\sigma = 40\text{nT}$, might be an underestimate for the B_{θ}^{ion} and B_{ϕ}^{ion} components. Applying individual a-priori errors to the different components could be investigated in future work.

Furthermore, an inclusion of induction in the forward model should be considered in order to account for the induced currents in the mantle. This might help improve the fit to ground station data, and it could also be considered to use ground data as input to the inversions.

As described in section 5.4 there seem to be something missing in the model that causes the absence of signals. It could be considered to include new input parameters e.g. time from the substorm onset, or a measure of the amount of open magnetospheric flux or the size of the polar cap.

Conclusion

In this thesis models of the magnetic fields produced by electrical currents in the ionosphere during magnetic disturbed times have been constructed. This was done by deriving a climatological model of the average ionospheric currents for given input parameters using data from the satellite Swarm A and auxiliary data in the form of measurements of the solar wind and interplanetary magnetic field interpolated in time to match the timestamps of the Swarm data. The modelling procedure was based on the methods of AMPS [Laundal, Finlay, Olsen, and Reistad 2018] and was carried out in the Python software Multifit [Kloss 2021]. In addition to the standard solar wind driving input for AMPS the *SML* index was introduced in the modelling procedure to better account for variations in the auroral electrojet activity. Apart from being a model input *SML* was also used to select magnetic disturbed times in the dataset through the method proposed by Newell and Gjerloev 2011.

The results of the model, shown in chapter 4, showed that under typical conditions the model was able to fit the radial component of the ionospheric field B_r^{ion} within 40-50nT. The prediction of B_θ^{ion} and B_ϕ^{ion} had significantly higher residuals, than the predictions for B_r^{ion} , especially near the poles. It was explained that the field-aligned currents (FAC), which are challenging to model as they can be small scale and highly dynamic, strongly affected B_θ^{ion} and B_ϕ^{ion} but had a less effect on B_r^{ion} which was mainly dominated by signals coming from the divergences-free currents (DFC).

During a large substorm event plots of the FACs and DFCs were produced and it was found that the DFC went from having a complex pattern to being more aligned with the FAC and gain a more structured pattern and a higher amplitude. The positive DFC values gather around the downward FAC in region 1 while the negative DFC values gather around the upward FAC. Plots of the horizontal sheet currents during the same substorm showed that the maximum current density moved down towards lower magnetic latitudes during the course of the substorm.

Comparisons to independent satellite data from Swarm A and ground observatory data were conducted. For the satellite data it was found that the model displayed a similar pattern as the data but failed to reach the same field strength amplitudes. It was suggested to include satellite data, in the modelling procedure, from more years in order to train the algorithm to model substorms based on a broader range of events. The comparison to

ground observatory data showed some large deviations between model and data. It was suggested that the differences to the ground observatory data, were likely due to unresolved small scale behaviour or non-typical dynamical features in any given substorm as well as un-modelled induced currents in the mantle. It was suggested that future models should attempt to implement ground observatory data in the modelling scheme.

The influence of the *SML* index, on the model, was investigated. Here it was found that *SML* strongly affected the amplitude of FAC and the pattern of the DFC. Since the *SML* index is a measure of the auroral electrojet activity it is connected to the substorm current wedge, involving both FAC and the westward substorm electrojet, making it a crucial factor in the ionospheric modelling.

A number of suggestions and recommendations for future work have been made. It was concluded that changing the selection scheme to include more data from classified substorms did not affect the modelling significantly and it was instead recommended to include data from a longer time period and data from different satellites especially CHAMP since it collects data from lower altitudes closer to the E-layer currents. The histograms of the residuals between model predictions and data showed Laplacian distributions and it was recommended to consider using Laplacian weighting-scheme instead of the used Huber weighting in the robust least squares inversion scheme. It was also noted that the adopted simple a-priori data error, $\sigma = 40\text{nT}$, might have been an underestimate for the components B_{θ}^{ion} and B_{ϕ}^{ion} and thus it was recommended to investigate the influence of individual a-priori error estimates for different field components. The absence of some observed signals, in particular for the ground observatories, suggested that the model was not complete, thus it was recommended to consider the inclusion of new input parameters e.g. time from substorm onset, measure of open magnetospheric flux, or size of polar cap in future models.

Bibliography

- Laundal, K., C. Finlay, N. Olsen, and J. Reistad (2018). “Solar Wind and Seasonal Influence on Ionospheric Currents From Swarm and CHAMP Measurements”. In: *Journal of Geophysical Research: Space Physics* 123. Full paper. DOI: <https://doi.org/10.1029/2018JA025387>.
- Kloss, C. (2021). “Geomagnetic field modelling and polar ionospheric currents”. PhD thesis. DTU.
- Olsen, N. and C. Stolle (2012). “Satellite Geomagnetism”. In: *Annu. Rev. Earth Planet. Sci.* Chap. 40(1):441-465. DOI: [10.1146/annurev-earth-042711-105540](https://doi.org/10.1146/annurev-earth-042711-105540).
- Kelley, M. (2007). “The Earth’s Ionosphere. Plasma Physics and Electrodynamics”. In: vol. 2nd Edition. Academic Press, Amsterdam, San Diego, London.
- Baumjohann, W. and R. Nakamura (2007). “Magnetospheric Contributions to the Terrestrial Magnetic Field”. In: *Elsevier B.V.* Volume 5, p. 77–91. DOI: [10.1016/B978-0-444-53802-4.00097-X](https://doi.org/10.1016/B978-0-444-53802-4.00097-X).
- Christensen, U. and J. Wicht (2015). “Numerical Dynamo Simulations”. In: *Treatise on Geophysics* 8.2nd edition, pp. 245–277.
- Constable, S. (2015). “Induction Studies”. In: *Treatise on Geophysics* 5.2nd edition, pp. 219–254.
- “Lecture notes, MSc Geomagnetism course, DTU” (Jan. 2021). Lecture notes. URL: <https://learn.inside.dtu.dk/d2l/le/content/59429/viewContent/220058/View>.
- Cowley, S. W. H. (2000). “Magnetosphere-ionosphere interactions: A tutorial review”. In: *Magneto- spheric Current Systems*, pp. 91–106. DOI: [10.1029/gm118p0091](https://doi.org/10.1029/gm118p0091).
- Milan, S. et al. (2017). “Overview of Solar Wind–Magnetosphere–Ionosphere–Atmosphere Coupling and the Generation of Magnetospheric Currents”. In: *Space Science Reviews* 206, pp. 547–573.
- Kepko, L. et al. (2015). “Substorm Current Wedge Revisited”. In: *Space Sci Rev* 190:1–46. DOI: [10.1007/s11214-014-0124-9](https://doi.org/10.1007/s11214-014-0124-9).
- Newell, P. and J. Gjerloev (2011). “Evaluation of SuperMAG auroral electrojet indices as indicators of substorms and auroral power”. In: *Journal of Geophysical Research* 116, Full article.
- Richmond, A. (1995). “Ionospheric electrodynamics. Handbook of Atmospheric Electrodynamics”. In: vol. 2. CRC Press, Boca Raton. Chap. 9.
- Laundal, K. (2018). *The average magnetic field and polar current system (AMPS) model*. URL: <https://klaundal.w.uib.no>.
- Olsen, N., H. Lühr, et al. (2014). “The CHAOS-4 geomagnetic field model”. In: *Geophysical Journal International* 197, pp. 815–827. DOI: [10.1093/gji/ggu033](https://doi.org/10.1093/gji/ggu033).

- Finlay, C. et al. (2020). “The CHAOS-7 geomagnetic field model and observed changes in the South Atlantic Anomaly”. In: *Earth Planets Space* 72 156. DOI: <https://doi.org/10.1186/s40623-020-01252-9>.
- Laundal, K., C. Finlay, and N. Olsen (2016). “Sunlight effects on the 3D polar current system determined from low Earth orbit measurements”. In: *Earth, Planets and Space* 68:142. DOI: 10.1186/s40623-016-0518-x.
- ESA Swarm mission: An overview* (2021). URL: http://www.geomag.bgs.ac.uk/education/swarm%5C_overview.html.
- Swarm instruments* (2012). URL: https://www.esa.int/ESA_Multimedia/Images/2012/11/Swarm_instruments_side_view.
- Kauristie, K. et al. (2017). “On the usage of geomagnetic indices for data selection in internal field modelling”. In: *Space Science Reviews* 206.0038-6308, pp. 61–90.
- SuperMAG* (2021). URL: <https://supermag.jhuapl.edu/info/>.

Model construction and setup

A.1 Regularisation of FAC

In order to create the best possible models a regularisation of the FAC needs to be established. This is done by running a series of test models where the regularisation parameter is varied. In this thesis regularisation parameters between $1\text{e}1\text{nT}^{-2}$ and $1\text{e}8\text{nT}^{-2}$ were tried. Table A.1 displays the normalised misfit and model norm for each of the eight model runs.

$\alpha^2 \text{ [nT]}^{-2}$	N	Misfit norm.	Model norm. $[\text{nT}]^2$	n	m
1e1	501289	1.2915	9.3820e-02	65	3
1e2	501289	1.3156	7.8680e-03	65	3
1e3	501289	1.3351	1.6890e-03	65	3
1e4	501289	1.3847	2.1409e-04	65	3
1e5	501289	1.4378	1.5606e-05	65	3
1e6	501289	1.4731	2.7756e-06	65	3
1e7	501289	1.5270	9.5367e-07	65	3
1e8	501289	1.8137	1.5209e-07	65	3

Table A.1: Eight runs of the model with different regularisation parameters. The table displays the number of data N , regularisation parameter α^2 , normalised misfit, model norm for the FAC, truncation degree n , and truncation order m for the FAC each model was produced after 7 iterations.

Figure A.1 shows the L-curve that is produced by plotting the model norm, on a logarithmic scale, against the normalised misfit, on a linear scale. The red circle marks the point of maximum curvature also known as the best trade off between good data fit and model complexity. The title of the plot displays the regularisation parameter for this point.

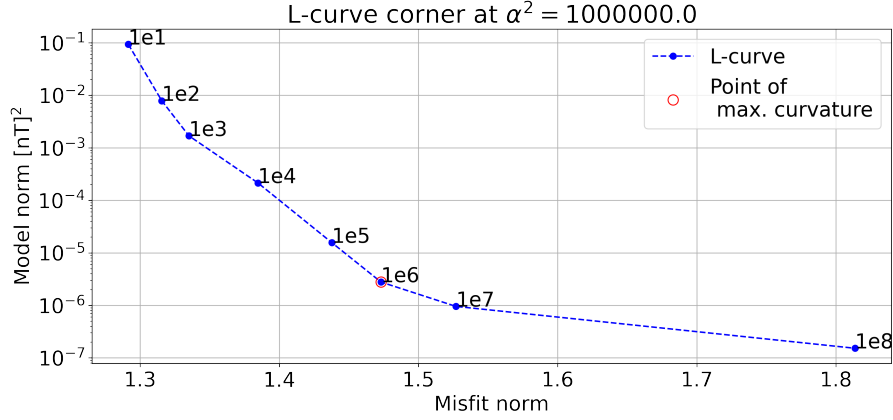
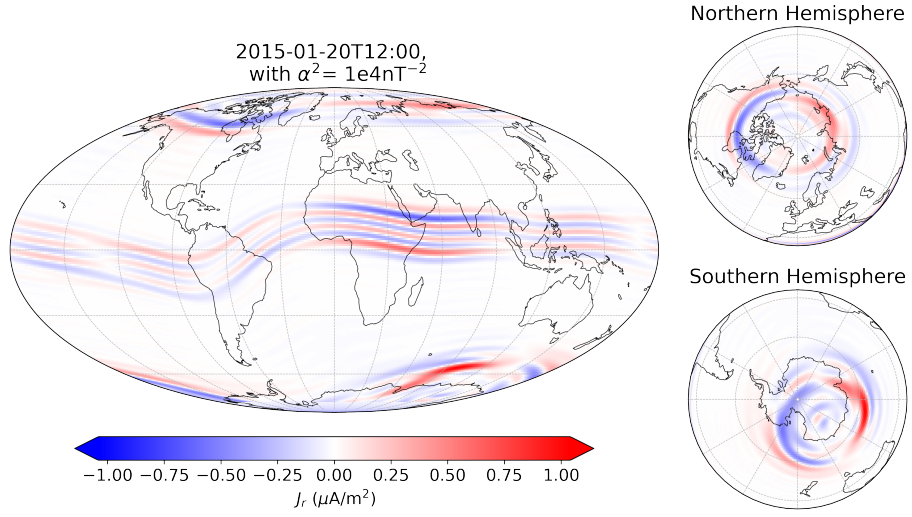
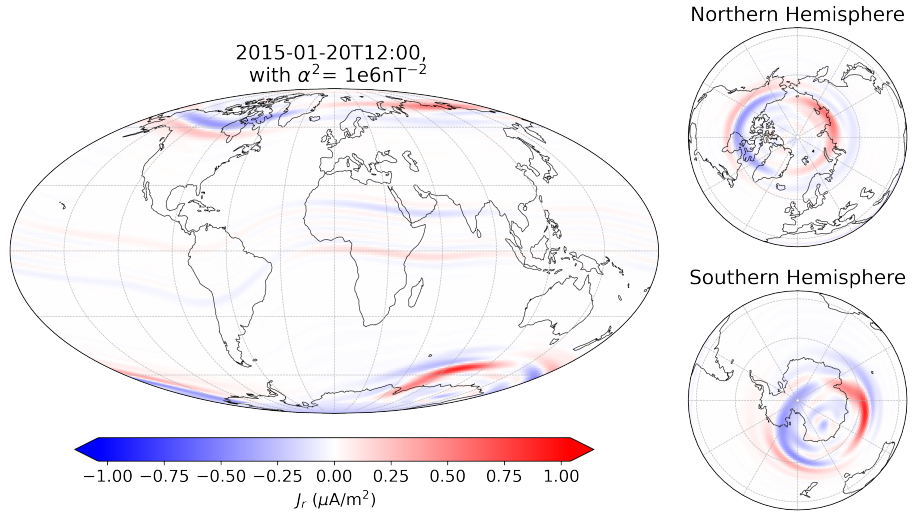


Figure A.1: An L-curve for the different regularisation parameters for the FAC. The red circle marks the point of maximum curvature on the graph and the corresponding regularisation parameter α^2 is printed in the title of the plot.

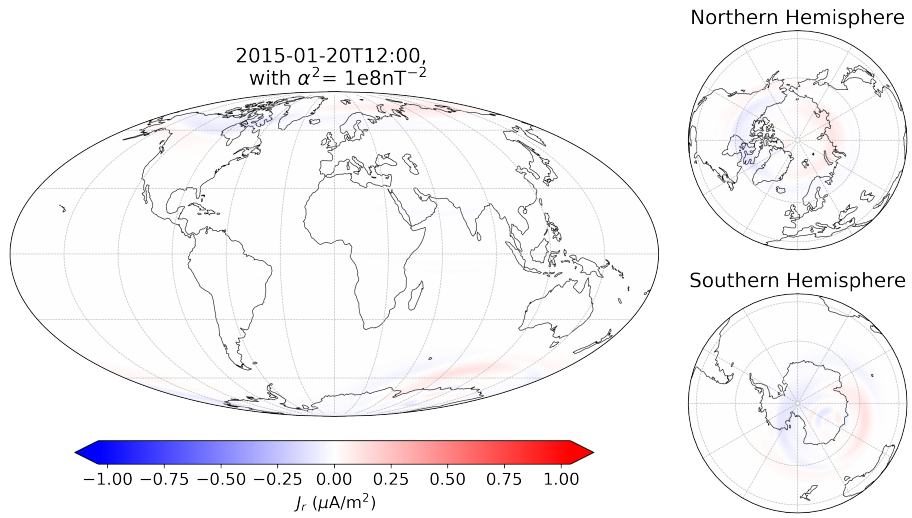
As figure A.1 displays the L-curve does not have a sharp knee hence it is hard to choose a perfect regularisation parameter. Figure A.2 shows three examples of the current density J_r for the FAC for a regularisation of $1e4nT^{-2}$ (A.2a), $1e6nT^{-2}$ (A.2b), $1e8nT^{-2}$ ((A.2c)). This figure reveals the effect of the regularisation. In figure A.2a strong clear patterns at, and close to, equator appears with changing polarity. As the regularisation increases this pattern gets damped. Figure A.2b shows a damped pattern around equator while still maintaining moderately strong currents in the polar regions. In figure A.2c the pattern around equator has been damped but so have the amplitude of the currents in the polar regions. Since we do not wish to attenuate the signal coming from the polar currents a compromise must be made. Thus a regularisation parameter of $1e6nT^{-2}$ is chosen based on figure A.1 and A.2.



(a)



(b)



(c)

Figure A.2: Three examples of the current density J_r modeled with a regularisation of $1\text{e}4\text{nT}^{-2}$ (a), $1\text{e}6\text{nT}^{-2}$ (b), $1\text{e}8\text{nT}^{-2}$ (c) at 20/01/2015 12:00 UTC and in a height of 110 km.

A.2 Choice of truncation level m

The regularisation parameter was found by running eight different models with fixed truncation levels at $m_{FAC} = 3$, $m_{DFC} = 3$, $n_{FAC} = 65$, and $n_{DFC} = 45$. These levels were chosen based on the previous AMPS model truncation levels. It was also tested whether or not these truncation levels were adequate. This was done by running three models with a fixed regularisation of $1\text{e}6\text{nT}^{-2}$ where m_{FAC} and m_{DFC} was varied simultaneously. Table A.2 displays the normalised misfit for each of the three test models. As expected, the misfit appears to drop slightly as the truncation levels m_{FAC} and m_{DFC} increase.

Figure A.3 shows three polar plots of the FAC and DFC with respect to clock angle for the three test models. There appears to be a small change in amplitude for both currents. As the truncation levels increase so does the complexity of the DFC-pattern. Table A.2 also indicates that the models with higher truncation levels need longer time to converge than the model for $m_{DFC}, m_{FAC} = 3$.

To avoid the risk of a model that is unnecessarily complex and is computationally slow the truncation level of $m_{DFC}, m_{FAC} = 3$ was chosen and kept fixed for the results presented in the thesis. This is justified since the normalised misfit is not changing much for the truncations tested.

m_{FAC}	m_{DFC}	n_{FAC}	n_{DFC}	Misfit norm.	$ \delta\mathbf{m} / \mathbf{m} $
3	3	65	45	1.4731	$1.0396\text{e-}02 \sim 1.04\%$
4	4	65	45	1.4458	$1.1482\text{e-}02 \sim 1.15\%$
5	5	65	45	1.4154	$1.3097\text{e-}02 \sim 1.31\%$

Table A.2: Displayed are the different truncation levels of the model vector \mathbf{m} and the corresponding normalised misfit for three different model runs. $\delta\mathbf{m}$ is the change in model parameter from one iteration to the next. The models were produced with a regularisation parameter of $1\text{e}6\text{nT}^{-2}$ and a run of 7 iterations each.

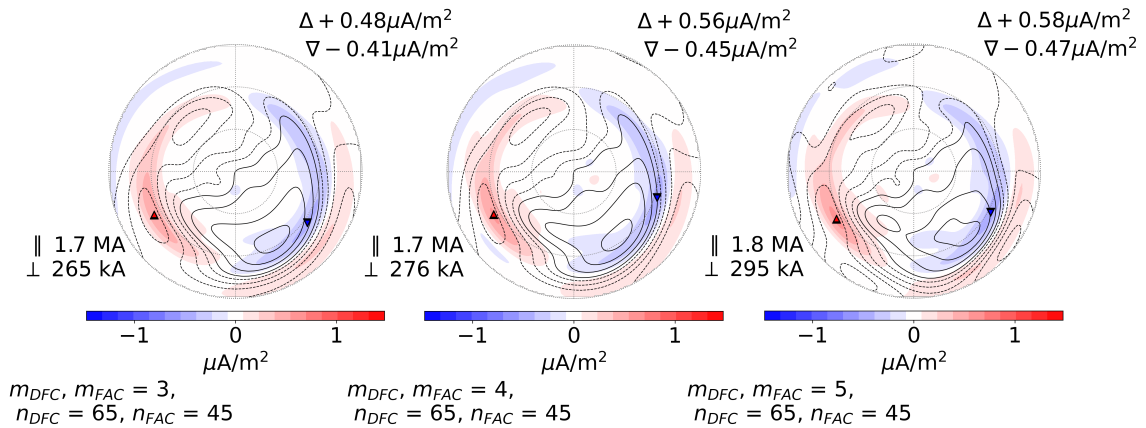


Figure A.3: Plots of the FAC and DFC with respect to clock angle, under typical conditions, for three different truncation levels of m_{DFC} and m_{FAC} . Here $n_{DFC} = 45$ and $n_{FAC} = 65$ for all three plots.

A.3 Choice of truncation level n

The choice of truncation levels n_{DFC} and n_{FAC} is based on three test-models each made from 2 iterations with an a-priori error of 30nT and a regularisation parameter of $1e6nT^{-2}$. Increasing the truncation levels also increases the computation time and hence only two iterations are run. The convergence, normalised misfit, and truncation levels for these tests can be seen in table A.3. The change-rate is rather high and that is due to the few iterations run, it is also seen that increasing the truncation level also increases the change-rate. Hence higher truncation levels requires a higher number of iterations in order for the model to converge.

m_{FAC}	m_{DFC}	n_{FAC}	n_{DFC}	Misfit norm.	$ \delta\mathbf{m} / \mathbf{m} $
3	3	60	40	1.4250	3.0458e-01 \sim 30.5%
3	3	65	45	1.4227	3.4355e-01 \sim 34.4%
3	3	70	50	1.4209	3.8380e-01 \sim 38.4%

Table A.3: Displayed are the different truncation levels n_{DFC} and n_{FAC} and the corresponding normalised misfit for three different model runs. $\delta\mathbf{m}$ is the change in model parameter from one iteration to the next. The models were produced with a regularisation parameter of $1e6nT^{-2}$ and a run of 2 iterations each.

In figure A.4 are shown the FACs and DFCs for the three test-models with varying truncation levels. The FACs and DFCs do not change significantly much when increasing the truncation levels n_{FAC} and n_{DFC} . The normalised misfit seen in table A.3 seems to decrease, but only slightly, with increasing truncation level. Because we wish to maintain a somewhat simple model with a high accuracy truncation levels of $n_{FAC} = 65$ and $n_{DFC} = 45$ are chosen. By increasing the truncation levels we also increase the complexity and the computation time of the model which, in the case of this thesis, has been chosen not to do due to time constraints.

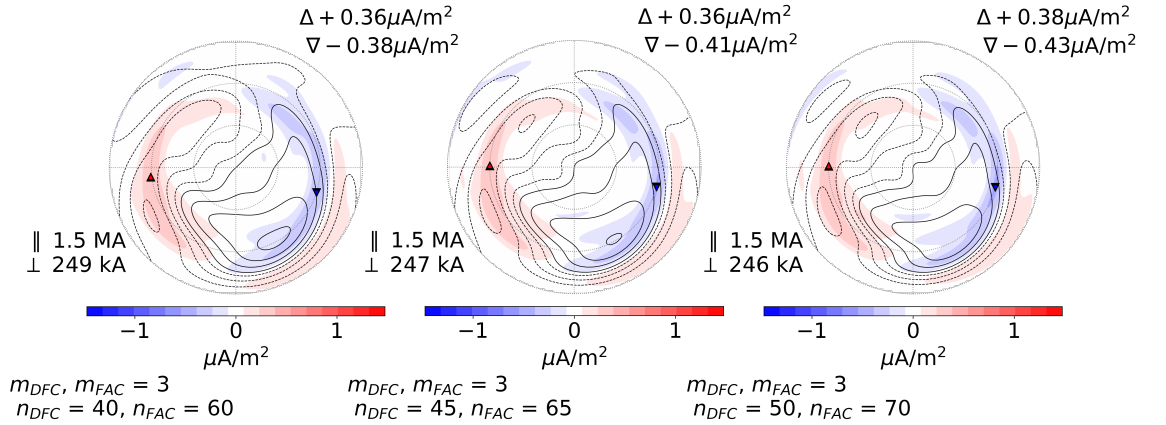


Figure A.4: Plots of the FAC and DFC with respect to clock angle under typical conditions for three different truncation levels of n_{DFC} and n_{FAC} . Here $m_{DFC} = 3$ and $m_{FAC} = 3$ for all three plots.

A.4 Test of convergence

In this section it will be investigated how many iterations are needed in order to obtain a good convergence. For this a test with a regularisation parameter of $1e6(nT)^{-2}$ and truncation levels of $m_{\text{FAC}} = 3$, $m_{\text{DFC}} = 3$, $n_{\text{FAC}} = 65$, and $n_{\text{DFC}} = 45$ is made. The normalised misfit and $\|\delta\mathbf{m}\|/\|\mathbf{m}\|$ of the last 7 to 10 iterations are shown in table A.4.

$\|\delta\mathbf{m}\|/\|\mathbf{m}\|$ is a measure of convergence. $\delta\mathbf{m}$ represents the change in model parameter from one iteration to the next. To say that a model has converged the following must be satisfied: $\|\delta\mathbf{m}\| \ll \|\mathbf{m}\|$. It is seen from table A.4 that this is the case for the last 4 iterations. The 7th iteration however seems to have the highest value of both misfit and $\|\delta\mathbf{m}\| \ll \|\mathbf{m}\|$ which indicates that the model has not yet reached a proper convergence level.

The rate at which $\|\delta\mathbf{m}\|/\|\mathbf{m}\|$ is decreasing from iteration to iteration is dropping which indicates that it has reached a plateau. By including more iterations $\|\delta\mathbf{m}\|/\|\mathbf{m}\|$ would be smaller however there are no indications that the misfit would change significantly. Thus I fix the number of iterations to 10 for the modelling procedure throughout this thesis.

Iteration number	$\ \delta\mathbf{m}\ /\ \mathbf{m}\ $	Misfit norm.
7	$1.0396\text{e-}02 \approx 1.04\%$	1.4731
8	$6.1493\text{e-}03 \approx 0.61\%$	1.4730
9	$3.8351\text{e-}03 \approx 0.38\%$	1.4730
10	$2.4704\text{e-}03 \approx 0.25\%$	1.4730

Table A.4: The last four iterations for a model with a regularisation of $1e6nT^{-2}$, a-priori error of $30nT$, and truncation levels of $m_{\text{FAC}} = 3$, $m_{\text{DFC}} = 3$, $n_{\text{FAC}} = 65$, and $n_{\text{DFC}} = 45$ is shown.

A.5 Test of a-priori data error

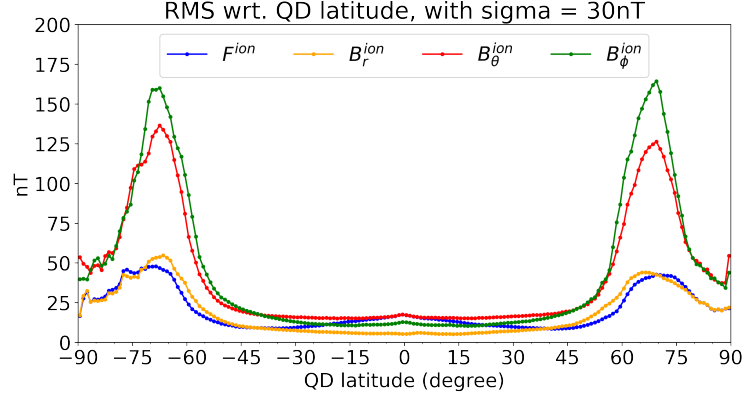
σ is a measure of data errors. For all the above models σ was fixed to $30nT$. For the final model however, a σ of $40nT$ is chosen. This is based on three test models where σ was varied. Table A.5 displays the settings of these models.

It is seen that a model with $\sigma = 100nT$ will converge faster than a models with lower σ values. However by increasing σ we also damp the amplitude of the signal in particular at the poles which we would like to avoid. However with a low value of σ we risk having a model that will not converge and hence we need to increase σ .

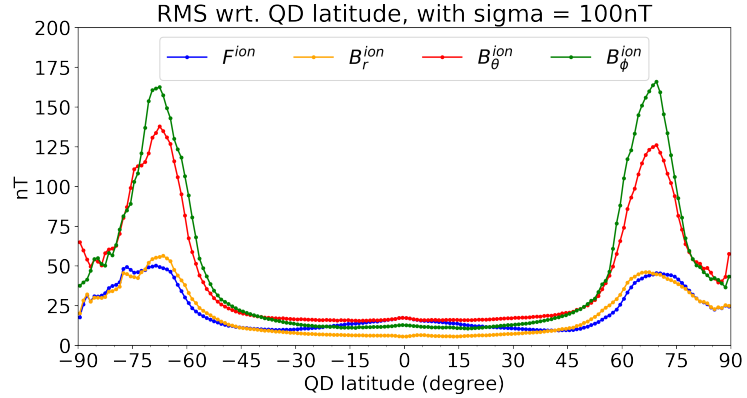
Figure A.5 shows two plots of the RMS for the residuals between model prediction and Swarm data with respect to QD-latitude for a-priori data errors of $30nT$ (A.5a) and $100nT$ (A.5b). Despite the difference in a-priori error the two plots do not deviate significantly much from each other. This means that a higher σ does not necessarily increase the model accuracy. In figures it is seen that B_r^{ion} and F^{ion} can be fitted within $40nT$ at the poles. Based on these plots and the convergence of the models a σ -value of $40nT$ is chosen.

σ (nT)	α^2 (nT ⁻²)	Total iteration number	$(m_{DFC},$ $m_{FAC})$	$(n_{DFC},$ $n_{FAC})$	Misfit norm.	$ \delta\mathbf{m} / \mathbf{m} $
30	1e6	10	(3, 3)	(45, 65)	1.4730	2.4704e-03 \approx 0.25%
50	1e6	10	(3, 3)	(45, 65)	0.7626	1.3253e-03 \approx 0.13%
100	1e6	10	(3, 3)	(45, 65)	0.2946	5.0287e-04 \approx 0.05%

Table A.5: The results of three model runs with varying a-priori data error σ .



(a)



(b)

Figure A.5: Plots of the RMS with respect to QD-latitude for the models $\sigma = 30\text{nT}$ (a) and $\sigma = 100\text{nT}$ (b).

A.6 Construction of Model B

Model B makes use of the same auxiliary data obtained from Swarm A as Model A. The data is from 01/01/2014 to 31/12/2017. The difference between Model A and Model B is the substorm selection criteria.

Instead of using the change in *SML* value Model B uses a *SML*-threshold. The *SML*-threshold is a measure of the restored *SML* value. In this model the threshold is set to 50% of the onset *SML* value.

Each onset, located in the dataset, will in Model B result in a substorm. The minimum duration of a substorm is set to 30min with means that the data selection method includes data for all values that are characterised as onset and values 30min after the substorm onset. If the *SML*-threshold of 50% of the *SML* value is reached after 30min the algorithm stops and does not include more datapoints from this substorm and moves on to the next substorm onset. If the threshold is not reached the algorithm will continue on including data until the threshold is reached or after 3hr have passed.

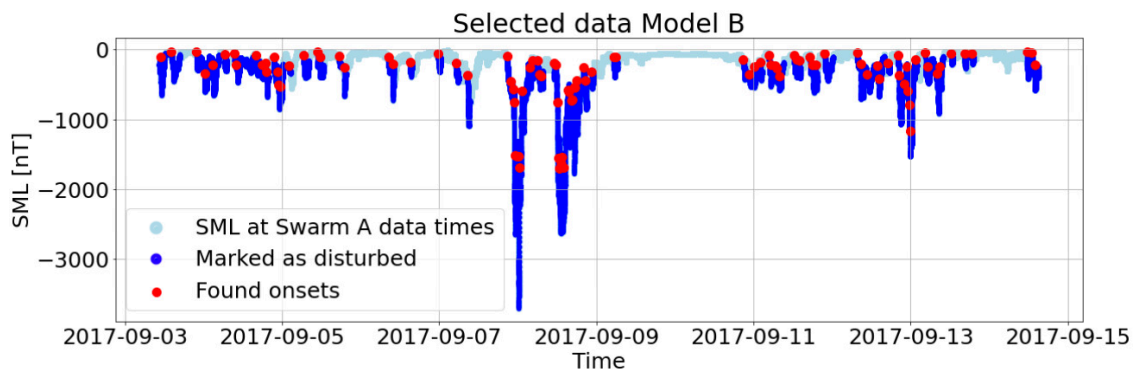


Figure A.6: A timeseries of *SML* indices for Swarm A data times for 03/09/2015 - 15/09/2015. The red dots represents the onsets found using the algorithm described for Model B while the dark blue dots denotes the selected disturbed data. The same timeseries has been plotted for Model A see figure 3.6.

An example of the selection criteria is shown in figure A.6. It is clearly seen how this model includes more datapoints. About 17% of the original datafile is included in the construction of Model B due to this selection scheme. This results in a better global coverage.

Appendix **B**

Scripts

Table B.1 displays the scripts used to derive the ionospheric current models, process the datafiles, and visualise the figures shown throughout this thesis. All scripts can be found in the zip-folder, called "Scripts", submitted along with this thesis.

	Name of script	Short description
Data processing:		
	driver.py	Python script used for model derivation. The script contains data configuration, dataload function, and model specification e.g. truncation degree, robust weighting, a-priori error estimate, and regularisation.
	add_external_parameters.py	Python script that collects external solar driving parameters and interpolates them to fit Swarm data times.
	dSML_Selection.ipynb	Data selection script for Model A based on the rate of change of SML.
	Threshold_Selection.ipynb	Data selection script for Model B based on a SML-threshold.
	CleanMyFile.ipynb	Removes NaN-values and large outliers.
	PlotCoef.ipynb	Distributions for different data variables in the "cleaned" datafile.
Test of model setup:		
	Regularization_FAC.ipynb	Comparison of models with different regularisations of FAC used in section A.1.
	Truncation_dependance.ipynb	Comparison of models with different truncation levels of n and m for the DFC and FAC used in section A.2 and A.3.
	Sigma_test.ipynb	Comparison of models with different a-priori data errors used in section A.5.
Visualisation of results:		
	FinalResults.ipynb	Containing plotting commands used to produce the plots seen in section 4.1.
	ResultsComparisons.ipynb	Containing plotting commands for all figures shown in section 4.2 - 4.4.

Table B.1: Name and short description of all the scripts used to derive the models and visualise the figures shown in this thesis. All scripts can be found in the uploaded zip-folder submitted along with this thesis.

Technical
University of
Denmark

Elektrovej, Building 327
2800 Kgs. Lyngby
Tlf. 4525 9500

www.space.dtu.dk